

# Rate and State Friction as a Spatially Regularized Transient Viscous Flow Law

Casper Pranger<sup>1,2</sup>, Patrick Sanan<sup>2</sup>, Dave A. May<sup>3</sup>, Laetitia Le Pourhiet<sup>4</sup>,  
Alice-Agnes Gabriel<sup>1</sup>

<sup>1</sup>Ludwig-Maximilians Universität München (LMU), Theresienstrasse 41, 80333 München, Germany.

<sup>2</sup>Institute of Geophysics, ETH Zurich, Sonneggstrasse 5, 8092 Zurich, Switzerland.

<sup>3</sup>Scripps Institution of Oceanography, UC San Diego, 9500 Gilman Drive, La Jolla, CA 92093, USA.

<sup>4</sup>Sorbonne Université, CNRS-INSU, Institut des Sciences de la Terre Paris, IStEP UMR 7193, F-75005,  
Paris, France

## Key Points:

- We reformulate the empirical rate and state friction law as a bulk viscous flow law in terms of anelastic shear strain rate.
- We show how mesh independence is achieved by including a gradient-like non-local anelastic shear strain rate equivalent.
- We show analytically and numerically that the proposed continuum model closely reproduces existing results of rate and state friction.

**Abstract**

The theory of rate and state friction unifies field, laboratory, and theoretical analysis of the evolution of slip on natural faults. While the observational study of earthquakes and aseismic fault slip is hampered by its strong multi-scale character in space and time, numerical simulations are well-positioned to link the laboratory study of grain-scale processes to the scale at which rock masses move. However, challenges remain in accurately representing the complex and permanently evolving sub-surface fault networks that exist in nature. Additionally, the common representation of faults as interfaces may miss important physical aspects governing volumetric fault system behavior. In response, we propose a transient viscous rheology that produces shear bands that closely mimic the rate- and state-dependent sliding behavior of equivalent fault interfaces. Critically, we show that the expected tendency of the continuum rheology for runaway localization and mesh dependence can be halted by including an artificial diffusion-type regularization of anelastic strain rate in the softening law. We demonstrate analytically and numerically using a simplified fault transect that important aspects of the frictional behavior are not significantly affected by the introduced regularization. Any discrepancies with respect to the interfacial description of fault behavior are critically evaluated using 1D numerical velocity stepping and spring-slider experiments. Since no new physical parameters are introduced, our model may be straightforwardly used to extend the existing modeling techniques. The model predicts the emergence of complex patterns of shear localization and delocalization that may inform the interpretation of complex damage distributions observed around faults in nature.

**Plain Language Summary**

How, where, and when earthquakes nucleate is one of the great questions in science and society that, despite steady progress, has hardly been answered to any practical degree. Based on field observations, laboratory experiments, and theoretical work it is believed that a cocktail of escalating mechanical, chemical, and thermal grain-scale processes cause the sudden and rapid onset of earthquakes. The net effect of these processes are characterized by an immediate strengthening and a gradual weakening response to deformation and are unified in simplified form in the theory of ‘rate and state friction’. This theory is commonly used in computer simulations of earthquake sequences. We point out that rate and state friction, unlike some physical theories of earthquake

rupture, does not incorporate a diffusion process such as for example heat conduction. We show the introduction of an artificial diffusion process can prevent the mathematical reduction of a fault zone to a two-dimensional interface while retaining the properties of the original friction law. This in turn enables simulation techniques that rely on an interface-free description of the earth and promise to provide new insights into the spontaneous organization of seismic and aseismic phenomena in developing fault zones.

## 1 Introduction

Over the second half of the last century the study of the sliding behavior of frictional surfaces, such as those believed to occur in the earth's crust, has led to a general understanding that it is governed by competition of stabilizing viscous-like effects and potentially destabilizing processes that affect the texture of the interface in a time-dependent manner and self-organize into periods during which the interface is arbitrarily close to elastic stick punctuated with periods of anelastic slip (Rabinowicz, 1958; Brace & Byerlee, 1966; Bowden & Tabor, 1966; Scholz et al., 1972; Ida, 1972; Dieterich, 1978; Ruina, 1980, 1983; Dieterich & Kilgore, 1994).

### 1.1 Rate- and State-dependent friction

This has led to the proposition of the phenomenological *rate- and state-dependent friction law* by Dieterich (1978, 1979a); Ruina (1980, 1983), which reads in its general form as

$$f = f_0 + a \log V + b \log \Theta. \quad (1)$$

In this law, the friction coefficient  $f$  is given by the linear combination of a reference friction coefficient  $f_0$ , a logarithmic contribution from dimensionless slip rate  $V$  multiplied by a coefficient  $a$ , and another logarithmic contribution from a dimensionless *state* variable  $\Theta$  multiplied by a coefficient  $b$ . All quantities are taken to be positive.

The rate-effect or *direct effect* is to a variable degree strengthening with increasing slip rate and thus exerts a stabilizing influence on the frictional interface for any strictly positive  $a$ . The *evolution effect* is to be governed by an evolution law that has the evolving steady state  $\Theta_{ss}V(t) = 1$ . Then, if  $b > a$ , this allows an externally loaded system with a frictional interface to move to a configuration with lower elastic strain energy and thus a frictional-mechanical instability may occur.

80 One of the most widely used state evolution laws is the *aging law* of Ruina (1980,  
81 1983), given by

$$82 \quad \dot{\Theta} = r_0 (1 - V\Theta), \quad (2)$$

84 with  $r_0$  a rate constant that is commonly expressed by dividing the reference velocity  
85  $v_0$  by a critical slip distance  $d_c$ . It should be noted that several other evolution laws that  
86 govern the state variable have been proposed. The most commonly cited contender is  
87 the *slip law* (Dieterich, 1979a; Ruina, 1980, 1983). In this work we do not consider it be-  
88 cause its functional form ( $\dot{\Theta} \propto \Theta V \log \Theta V$ ) is unfortunately not amenable to the type  
89 of analytical treatment that is performed. We note that rate and state friction captures  
90 only the first-order behavior of the stick-slip cycle and that laboratory experiments have  
91 brought to light many secondary effects (e.g. Ruina, 1983; Marone, 1998; Mair & Marone,  
92 1999; Chester, 1994; Passelègue et al., 2020).

93 Following Amonton’s law the friction coefficient is expressed as the ratio of shear  
94 stress  $\tau$  to normal stress  $\sigma$ , implying a cohesionless fault. It is further assumed that the  
95 fault is always critically loaded. This assumption is necessary because (1) degenerates  
96 at  $V = 0$ , but may also be realistic for faults in nature (Bak & Tang, 1989).

97 The rate and state friction law is frequently applied in numerical studies of fault  
98 slip, whether that be a study over the course of a single earthquake or a complex sequence  
99 of slip transients (e.g. Dieterich, 1979b; P. G. Okubo, 1989; Rice, 1993; Rice & Ben-Zion,  
100 1996; Ben-Zion & Rice, 1997; Lapusta et al., 2000; Lapusta & Liu, 2009; Rubin & Am-  
101 puero, 2005; Gabriel et al., 2012; Jiang & Lapusta, 2016; D. Li & Liu, 2017; Erickson  
102 et al., 2020). The use of interfacial friction laws in these models necessitates the treat-  
103 ment of faults as mesh features on which internal boundary conditions can be applied.  
104 It can be laborious to construct such meshes for non-trivial fault geometries, and the pro-  
105 cedure does not scale well with increasing fault network complexity. There is currently  
106 no established method to construct meshes with time-dependent geometry and topol-  
107 ogy reflecting an evolving fault system, but we refer to K. Okubo et al. (2019) for work  
108 in this direction. With some exceptions (e.g. D. Li & Liu, 2017; Sathiakumar et al., 2020;  
109 Perez-Silva et al., 2021) many studies focus on the already complex behavior of long-term  
110 sequences of slip transients on linear or planar faults in simple domains.

## 1.2 Continuum fault rheology

There is strong field and experimental evidence that faults in nature are not infinitely thin planes but consist of complex evolving networks of strongly localized shear zones within a wider region of damaged host rock (Tchalenko, 1970; Granier, 1985; Katz et al., 2004; Savage & Brodsky, 2011; Faulkner et al., 2011; Barth et al., 2013; Passelègue et al., 2016; Perrin et al., 2016; Locatelli et al., 2018, 2019; Pozzi et al., 2018, 2019, 2021; Ritter, Rosenau, & Oncken, 2018; Ritter, Santimano, et al., 2018; Ross et al., 2019). This knowledge has spurred a search for intermediate-scale continuum homogenizations of distributed micro-scale processes that obey the rate and state framework in a somewhat generalized sense. Currently proposed models focus on rheological feedback mechanisms involving temperature (Braeck & Podladchikov, 2007; John et al., 2009; Roubíček, 2014; Thielmann et al., 2015; Thielmann, 2018; Pozzi et al., 2021), grain size (Rozel et al., 2011; Thielmann et al., 2015; Thielmann, 2018; Barbot, 2019; Pozzi et al., 2021), porosity (Sleep, 1997; Niemeijer & Spiers, 2007; Chen & Spiers, 2016; Van den Ende et al., 2018), fluid pressure (Poulet et al., 2014; Veveakis et al., 2014; Alevizos et al., 2014; Rattetz, Stefanou, & Sulem, 2018; Rattetz, Stefanou, Sulem, Veveakis, & Poulet, 2018), damage (Lyakhovskiy et al., 2011; Lyakhovskiy & Ben-Zion, 2014b, 2014a; Lyakhovskiy et al., 2016; Kurzon et al., 2019, 2020), or combinations thereof. Continuum models employing a rate and state formulation with the slip rate and tractions replaced by strain rate and stress invariants have been developed by Herrendörfer et al. (2018) and applied to self-organizing fault systems in Preuss et al. (2019, 2020). Since the state of the subsurface is typically difficult to accurately characterize on a regional basis, these models are important to develop a generic understanding of the long-term evolution of seismogenic fault systems.

A problem commonly associated with strain softening rheologies without internal length scale is unconstrained localization (Hobbs et al., 1990). As a shear zone localizes to the scale of a mesh element or grid cell they become poorly resolved and cause mesh-dependence of the simulation. Models that possess an internal length scale perpendicular to the direction of shear may not suffer from this issue, provided that this length scale is resolved by the discretization. For example, as thermo-rheological feedback mechanism causes localization the heat diffusion term may gain prominence until localizing and delocalizing (diffusing) influences find a balance. Unfortunately some of the proposed fault rheologies don't possess an internal length scale, and some possess one that has physical meaning and can't be changed without changing the behavior of interest. If such a

144 physical length scale is very small in nature, then that may place insurmountable con-  
 145 straints on the mesh resolution in two- or three-dimensional regional simulations. A few  
 146 models *do* contain a controllable internal length scale; these are the unified rate and state  
 147 friction theory of Sleep (1997) and the damage-breakage rheology of Lyakhovsky and Ben-  
 148 Zion (2014b, 2014a); Lyakhovsky et al. (2016); Kurzon et al. (2019, 2020).

### 149 **1.3 Objective**

150 In summary, we state the need for a rigorous treatment of a continuum framework  
 151 in which Dieterich–Ruina-type rate and state friction can be embedded based on the fol-  
 152 lowing observations:

- 153 1. Rate and state friction is a useful and powerful homogenization of the complex  
 154 micro-scale processes that give rise to slip transients in nature.
- 155 2. Numerical modeling exploration of the complex and evolving relation that fault  
 156 networks have with their tectonic environment is hampered by the long-standing  
 157 challenges with mesh adaptive generation as well as lack of detailed knowledge of  
 158 the structure of the subsurface.
- 159 3. The description of fault friction as a continuum process can be an elegant and prac-  
 160 tical way to avoid these problems provided they possess a controllable internal length  
 161 scale in order to produce sensible results given reasonable computational resources.
- 162 4. Much effort has been dedicated to understanding rate and state friction as an in-  
 163 gredient in numerical models – not all proposed continuum rheologies can equally  
 164 benefit from this.

165 In response, we develop a Dieterich–Ruina-type continuum reformulation of rate  
 166 and state friction that

- 167 1. possesses a controllable internal length scale  $\lambda$  that enforces a constraint on lo-  
 168 calization,
- 169 2. yields mesh-independent results once  $\lambda$  is sufficiently well resolved, and
- 170 3. retains the parameters to the interfacial friction (1) and evolution (2) laws and  
 171 yields similar trajectories of  $V$  and  $f$  for the same choice of parameter values.

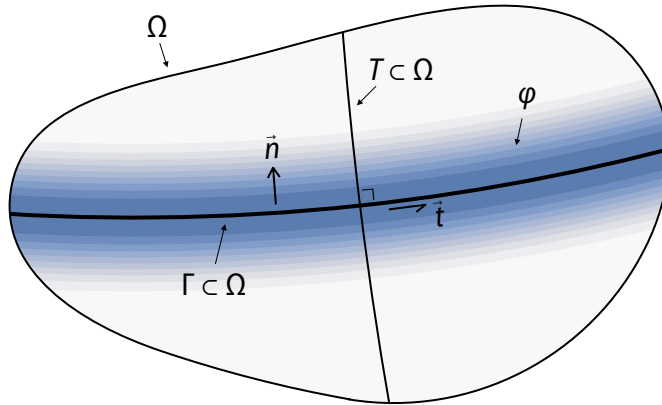


**Figure 1.** A region  $\Omega$  in the enclosing a portion of a fault interface  $\Gamma$ , with normal and tangent vectors  $\vec{n}$  and  $\vec{t}$  indicated. A transect  $T$  is drawn perpendicular to the fault. The fault interface may be substituted by a shear band on which anelastic shear strain is distributed according to  $\varphi(\vec{x})$ , as indicated by the colored contours.

172 The model we propose here bears close relation to the earlier works of Sleep (1997) and  
 173 Herrendörfer et al. (2018). Contrary to Sleep (1997) we refrain from in-depth discussion  
 174 of fault physics but concentrate on the introduced spatial regularization, which is also  
 175 a necessary extension of Herrendörfer et al. (2018).

176 In Section 2 we will motivate our choice of constitutive model, focusing on the for-  
 177 mal links between interfacial and continuum models. In Section 3 we will present our  
 178 equivalent continuum rate and state rheology. In Section 4 we build our rheology into  
 179 a numerical model of a simplified one-dimensional fault transect to demonstrate both  
 180 its localization and delocalization behavior as well as its similarities and differences with  
 181 respect to the original laws of Dieterich and Ruina. We close with a discussion and sum-  
 182 mary in Sections 5 and 6.

## 183 2 Material model and continuum mechanics

184 We will first describe how the existing interfacial description of rate and state fric-  
 185 tion can be embedded in a continuum mechanical framework with internal discontinu-  
 186 ities, and then generalize this to internal friction and distributed anelastic deformation  
 187 in an interface-free model.

## 2.1 A fault reference frame

We consider the immediate neighborhood  $\Omega \subset \mathbb{R}^3$  of a section of fault  $\Gamma \subset \Omega$  (Figure 1) that is described as the set of points belonging to a differentiable 2D manifold. We invoke the existence of a surjective function  $\vec{x}_f(\vec{x})$  that maps a coordinate  $\vec{x} \in \Omega$  to its nearest Euclidian neighbor  $\vec{x}_f \in \Gamma$ . Next, we define the fault transect  $T(\vec{x}_f) \subset \Omega$  as the 1D curve that includes all the points  $\vec{x} \in \Omega$  that map to a particular fault coordinate  $\vec{x}_f \in \Gamma$ , in short  $T = \vec{x}_f^{-1}(\{\vec{x}_f\}) \subset \Omega$ . Finally, we let  $\hat{n}(\vec{x}) \in \mathbb{R}^3$ ,  $\vec{x} \in \Omega$  be a unit vector field locally tangent to the transecting curve  $T(\vec{x}_f(\vec{x}))$  and therefore normal to the fault.

The *state* of the body  $\Omega$  is described by a symmetric Cauchy stress tensor field  $\boldsymbol{\sigma}(t, \vec{x}) \in \mathbb{R}^3 \otimes \mathbb{R}^3$  and a velocity vector field  $v_0 \vec{v}(t, \vec{x}) \in \mathbb{R}^3$ . Their governing equations are stated after the introduction of some further scaffolding. Let  $t$  denote time.

We define the normal traction  $\sigma = -\hat{n} \cdot \boldsymbol{\sigma} \cdot \hat{n}$  (positive in compression), the shear traction vector  $\vec{\tau} = \boldsymbol{\sigma} \cdot \hat{n} + \sigma \hat{n}$ , and the shear traction magnitude  $\tau = \sqrt{\vec{\tau} \cdot \vec{\tau}}$ . The rupture process is most efficient when the slip rate vector  $\vec{V} \in \mathbb{R}^3$  is parallel to the in-plane shear traction vector  $\vec{\tau}$ , and so alongside the full velocity field  $\vec{v}$  we define a purely slip-induced velocity double couple field  $\vec{v}_{\rightleftharpoons}$  around the coordinate  $\vec{x}$  as

$$\vec{v}_{\rightleftharpoons}(t, \vec{x}) := \frac{1}{2} V(t, \vec{x}_f) \hat{t}(\vec{x}_f) \operatorname{sgn}(\hat{n}(\vec{x}_f) \cdot [\vec{x} - \vec{x}_f]), \quad (3)$$

with  $\hat{t} \in \mathbb{R}^3 := \vec{\tau} / \tau$  the unit tangent vector and  $\operatorname{sgn}$  the sign function, which has  $\operatorname{sgn}(0) = 0$ .

## 2.2 Assumptions

In the following, we will assume that continuum processes that occur around the fault are predominantly confined to the small neighborhood  $\Omega$ , which itself includes only a small section of a whole fault. The neighborhood  $\Omega$  is assumed to be sufficiently small that in-plane variations of fault properties such as state, slip rate, and curvature are negligible. This assumption comes at a loss of generality, especially around fault kinks, branches, and tips, but does not necessarily limit the applicability of our formulation. We will revisit this assumption in the Section 5.5 of the Discussion.

### 2.3 Generalization of a fault to a shear band

We now generalize the fault interface to a distributed shear band by substituting a smoothed step function  $\Phi = \Phi(t, x; \lambda_0) \in [-1, +1]$ ,  $\lambda_0 > 0$  (e.g.  $\Phi(t, x; \lambda_0) := \tanh(x/\lambda_0)$ ) for the sign function in (3). We require that the chosen function converges in a point-wise manner to the sign function as  $\lambda_0 \rightarrow 0^+$ , such that (3) can be seen as the result of taking the limit

$$\begin{aligned} \vec{v}_{\rightleftharpoons}(t, \vec{x}; \lambda_0) &:= \frac{1}{2}V(t, \vec{x}_f) \hat{t}(\vec{x}) \Phi\left(t, \hat{n} \cdot \left[\frac{\vec{x} - \vec{x}_f}{\lambda_0}\right]\right) \\ \vec{v}_{\rightleftharpoons}(t, \vec{x}) &:= \lim_{\lambda_0 \rightarrow 0^+} \vec{v}_{\rightleftharpoons}(t, \vec{x}; \lambda_0). \end{aligned} \quad (4)$$

Recognizing that fault slip is an anelastic process, the anelastic strain rate tensor  $\dot{\epsilon}_{-e}$  is defined to be the symmetric gradient  $\nabla^s$  of the (continuous) slip-induced velocity field  $\vec{v}_{\rightleftharpoons}(t, \vec{x}; \lambda_0)$ :

$$\begin{aligned} \dot{\epsilon}_{-e}(t, \vec{x}) &:= v_0 \nabla^s \vec{v}_{\rightleftharpoons}(t, \vec{x}; \lambda_0) := \frac{1}{2}v_0 [(\nabla \vec{v}_{\rightleftharpoons})^T + (\nabla \vec{v}_{\rightleftharpoons})](t, \vec{x}; \lambda_0) \\ &\approx \frac{1}{2} \frac{v_0}{\lambda_0} V(t, \vec{x}_f) \varphi\left(t, \hat{n} \cdot \left[\frac{\vec{x} - \vec{x}_f}{\lambda_0}\right]\right) [\hat{t} \otimes \hat{n} + \hat{n} \otimes \hat{t}](\vec{x}) =: \gamma_0 \gamma(t, \vec{x}) \hat{s}(\vec{x}). \end{aligned} \quad (5)$$

Here the *equivalent anelastic shear strain rate* (a scalar value) has been introduced as  $\gamma_0 \gamma(t, x) = v_0 V(t) \varphi(t, x)$ , with reference value  $\gamma_0 = v_0/\lambda_0$  and *strain rate distribution*  $\varphi(t, x; \lambda_0) = \partial_x \Phi(t, x; \lambda_0)$  (illustrated in blue shading in Figure 1). The symbol  $\hat{s}$  denotes the unit shear sense tensor  $\hat{s} = \frac{1}{2} [\hat{t} \otimes \hat{n} + \hat{n} \otimes \hat{t}]$ , and its *Frobenius norm*  $\|\hat{s}\| = \sqrt{\text{tr } \hat{s}^T \hat{s}} = 1/\sqrt{2}$ , which is an important property to maintain when generalizing  $\hat{s}$  later on because it is compatible with the interpretation of  $\gamma_0 \gamma$  as the fault-perpendicular derivative of fault-parallel velocity, i.e. as an accurate measure of simple shear. In the derivation of (5) the gradients of  $V$  and the orthonormal bases  $\hat{t}$  and  $\hat{n}$  have been dropped under the assumption set out in Section 2.2 that they are small compared to the gradient of  $\Phi$ . For this assumption to be met, the across-fault length scale  $\lambda_0$  must be small compared to the along-fault length scales that exists in the interfacial rate and state formulation.

Since the derivative of half a smoothed step function  $\frac{1}{2}\Phi(x) \in [-\frac{1}{2}, +\frac{1}{2}]$  has the properties of a distribution – is a non-negative and importantly integrates to unity over its domain – we may express the integral relation

$$\mathcal{V}(\gamma) := \gamma_0 \int_T \gamma(t, \vec{x}) dx = v_0 V(t, \vec{x}_f) \quad (6)$$

249 over the fault transect  $T$ , which is again compatible with the notion that  $\gamma_0\gamma$  is a mea-  
 250 sure of simple shear in the fault reference frame. We note that the above integral strictly  
 251 requires that all anelastic strain occurs over the length of the fault transect  $T$ , imply-  
 252 ing that the anelastic strain rate distribution has compact support in space. In practice  
 253 we can relax that requirement if said distribution is narrow and thin-tailed.

254 Subtracting the anelastic shear strain rate tensor  $\dot{\epsilon}_{-e}$  from the full strain rate ten-  
 255 sor  $\dot{\epsilon} = \nabla^s \vec{v}$  results in the elastic strain rate tensor. This additive decomposition of elas-  
 256 tic and anelastic strains is known as the Maxwell model. Application of Hooke's law of  
 257 linear elasticity to the elastic strain rate tensor leads to

$$258 \quad \dot{\sigma} = \mathbf{S} [\dot{\epsilon} - \gamma_0\gamma \hat{s}] \quad (7)$$

259  
 260 with fourth-order elastic stiffness tensor  $\mathbf{S}$  and the dot over a symbol denoting the time  
 261 derivative. The relation above is standard in the context of elasto-plasticity (e.g. Mühlhaus  
 262 & Aifantis, 1991), in which  $\gamma_0\gamma$  is known as the plastic multiplier and  $\hat{s}$  coincides with  
 263 the derivative of the magnitude of shear traction  $\tau$  with respect to the full stress ten-  
 264 sor  $\sigma$ . In this case  $\tau$  is to be interpreted as the *non-associated* plastic potential of a ma-  
 265 terial that does not undergo anelastic volume change.

266 For completeness we list ordinary differential equation that governs  $\vec{v}$ , the *momentum*  
 267 *balance equation*:

$$268 \quad v_0 \dot{\vec{v}} - \vec{g} = \rho^{-1} \nabla \cdot \sigma. \quad (8)$$

269  
 270 Here  $\vec{g}$  is the acceleration due to gravity and  $\rho$  the mass density. Gravity may be ignored  
 271 in the remainder of this work at no loss of generality and the inertial term  $\dot{\vec{v}}$  may be ig-  
 272 nored at *some* loss of generality under the assumption of static momentum balance.

## 273 **2.4 Plasticity and coordinate invariance**

274 For a spontaneously developing fault zone the shear and normal stress can not be  
 275 defined in relation to a known plane. Plasticity models avoid this problem through the  
 276 use of stress tensor invariants and scalar parameters. The Mohr-Coulomb plasticity model  
 277 generates anelastic shear strain parallel to the unit shear sense tensor  $\hat{s} = \frac{1}{2}(\hat{n} \otimes \hat{t} + \hat{t} \otimes$   
 278  $\hat{n})$ , in which  $\hat{t}$  makes an angle  $\phi = \tan^{-1} f$  with respect to the largest principal stress  
 279 axis  $\vec{\sigma}_1$ , and  $\hat{t}$  and  $\hat{n}$  form an orthogonal triad of vectors together with the intermediate  
 280 principal stress axis  $\vec{\sigma}_2$ . In other words, anelastic shear strain occurs in a plane perpen-

281 dicular to  $\vec{\sigma}_2$ . The corresponding cohesionless yield criterion is written as

$$282 \quad \sigma_1 - \sigma_3 = -\sin(\phi)(\sigma_1 + \sigma_3), \quad (9)$$

283  
 284 with  $\sigma_1$  and  $\sigma_3$  the magnitudes of the largest and smallest principal stresses  $\vec{\sigma}_1$  and  $\vec{\sigma}_3$ .  
 285 We note that the angle of a shear band that is generated does not need to be parallel  
 286 to the direction of shear strain (Vardoulakis, 1980; Vermeer, 1990; Kaus, 2010; Le Pourhiet,  
 287 2013), and moreover that a local change in friction is not expected to immediately al-  
 288 ter the macroscopic fault angle (e.g. Preuss et al., 2019).

289 In the Mohr-Coulomb model, the friction coefficient  $f$  of a yielding material may  
 290 be expressed as a function of the principal stresses  $\sigma_1$  and  $\sigma_3$  as

$$291 \quad f(\boldsymbol{\sigma}) = \frac{1}{2} \frac{\sigma_1(\boldsymbol{\sigma}) - \sigma_3(\boldsymbol{\sigma})}{\sqrt{\sigma_1(\boldsymbol{\sigma})\sigma_3(\boldsymbol{\sigma})}} \quad (10)$$

292  
 293 Herrendörfer et al. (2018) used the Drucker-Prager model (Drucker & Prager, 1952)  
 294 as a simple and smooth approximation to Mohr-Coulomb plasticity. The model is de-  
 295 fined in terms of the straightforwardly computable invariants

- 296 1. pressure  $p = -\frac{1}{3} \text{tr } \boldsymbol{\sigma}$ , and
- 297 2. effective shear stress  $\tau_e$  proportional to the *Frobenius norm* of the deviatoric stress  
 298 tensor  $\boldsymbol{\tau} := \boldsymbol{\sigma} + p\boldsymbol{\delta}$ , with  $\boldsymbol{\delta}$  the Kronecker delta:

$$299 \quad \tau_e := \frac{\|\boldsymbol{\tau}\|}{\sqrt{2}} = \sqrt{\frac{1}{2} \text{tr}(\boldsymbol{\tau}^T \cdot \boldsymbol{\tau})}. \quad (11)$$

300  
 301 In this model the existing definition of the unit shear sense tensor  $\hat{\boldsymbol{s}}$  is no longer appli-  
 302 cable because the unit vectors  $\hat{t}$  and  $\hat{n}$  are not known *a priori*, and are not even uniquely  
 303 constrained *a posteriori*. Keeping in line with plasticity theory,  $\hat{\boldsymbol{s}}$  is redefined as the stress  
 304 derivative of the non-associated plastic potential  $\tau_e$ :

$$305 \quad \hat{\boldsymbol{s}} := \frac{\partial \tau_e}{\partial \boldsymbol{\sigma}} = \frac{\boldsymbol{\tau}}{\tau_e}.$$

306  
 307 This definition still satisfies the criterion set out in the preceding section that  $\|\hat{\boldsymbol{s}}\| = 1/\sqrt{2}$ .

308 We calibrate the Drucker-Prager model to the Mohr-Coulomb model around a ref-  
 309 erence stress state  $\boldsymbol{\sigma}_0$  of simple shear combined with isotropic compression, which en-  
 310 compasses all stress states possible in 2D plane strain and may be considered the most  
 311 relevant stress state even in 3D tectonic settings. Let  $\vec{\sigma}_0$  be given in ordered principal

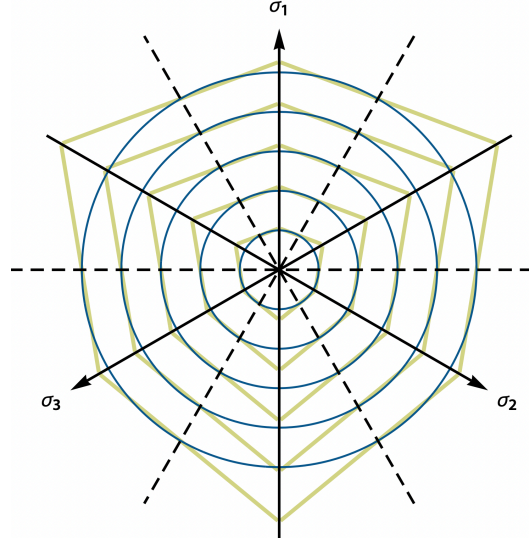


**Figure 2.** Comparison of Mohr-Coulomb (thick yellow lines) and Drucker-Prager yield envelopes (thin blue lines) at increments of pressure. The field of view is the octahedral plane of principal stress space. Projections of principal stress axes are indicated with arrows, and projections of planes of simple shear are indicated with dashed lines. A friction coefficient of 0.3 was used to generate this figure.

stress space by

$$\vec{\sigma}_0 := -p_0 \begin{bmatrix} 1 \\ 1 \\ 1 \end{bmatrix} + \tau_{e,0} \begin{bmatrix} +1 \\ 0 \\ -1 \end{bmatrix}.$$

At  $\vec{\sigma} = \vec{\sigma}_0$ , Mohr-Coulomb and Drucker-Prager measures of effective shear and normal stress coincide (up to a sign) and thus the Drucker-Prager model may be written as

$$\tau_e(\boldsymbol{\sigma}) = \sin(\phi) p(\boldsymbol{\sigma}). \quad (12)$$

Away from  $\vec{\sigma}_0$  (and towards a uniaxial stress state) the Drucker-Prager yield surface becomes an increasingly worse approximation to the Mohr-Coulomb yield surface (Figure 2). Higher-order approximations like the Willam-Warnke yield envelope (Ulm et al., 1999) may be considered too. The yield surfaces discussed in this section serve as part of a general model proposition – in the one-dimensional numerical experiments considered in this work only the two effective stresses of Amonton’s friction law are defined.

For a material that is known to be in a state of plastic yielding, the friction coefficient  $f = \tan \phi$  may also be expressed from (12) as a function of the stress tensor  $\boldsymbol{\sigma}$

327 as

$$328 \quad f(\boldsymbol{\sigma}) = \tau_e(\boldsymbol{\sigma}) [p(\boldsymbol{\sigma})^2 - \tau_e(\boldsymbol{\sigma})^2]^{-\frac{1}{2}}. \quad (13)$$

329

330 The friction coefficient  $f(\boldsymbol{\sigma})$  equals one when the pressure  $p(\boldsymbol{\sigma}) = 0$  and equals zero  
 331 when the effective stress  $\tau_e(\boldsymbol{\sigma}) = 0$ . The friction coefficient falls in the interval  $[0, 1]$  at  
 332 any state of stress  $\boldsymbol{\sigma}$ , but has discontinuous derivatives at aforementioned zeroes of  $p$  and  
 333  $f(\boldsymbol{\sigma})$ .

334 Despite adopting a plasticity framework to enforce the frictional yield constraint  
 335 we emphasise that the resulting model is still best regarded as ‘frictional viscous’ rather  
 336 than frictional plastic because it lacks a distinct boundary between yielding and non-  
 337 yielding states in space and time – the yield constraint (an equality, not an inequality)  
 338 is enforced everywhere and anytime, and at any stress.

### 339 **3 Continuum evolution law**

340 Our goal is to find a continuum state evolution law that produces nearly the same  
 341 history of loading and sliding as the original formulation of Dieterich and Ruina on a dis-  
 342 crete fault. Like  $V(t)$  is a ‘global’ measure of  $\gamma(t, x)$  over a fictitious fault transect  $T$ ,  
 343 we introduce a local variable  $\theta(t, x)$  of which  $\Theta(t)$  is a global measure. We target con-  
 344 tinuum friction and evolution laws expressed in terms of  $\gamma$  and  $\theta$  of the form

$$345 \quad f = f_0 + a \log \gamma + b \log \theta, \quad (14)$$

$$346 \quad \dot{\theta} = r_0 (c_2 - c_1 \mathcal{M}(\gamma) \theta), \quad (15)$$

347

348 with  $\mathcal{M}$  a smoothing operator that will be further elaborated in Section 3.3 and  $c_1$  and  
 349  $c_2$  additional coefficients that are required to calibrate (14) and (15) to their respective  
 350 interfacial equivalent. The local friction and evolution laws (14) and (15) retain the struc-  
 351 ture of their interfacial counterparts (1) and (2) and generalize the continuum formu-  
 352 lations of Sleep (1997) and Herrendörfer et al. (2018). We will revisit this connection in  
 353 the Section 5.4 of the Discussion. The targeted form of the continuum equations does  
 354 not come out of the blue. In coming sections we hope to make clear how it arises.

#### 355 **3.1 Analytical framework**

356 By

- 357 1. reorganizing the rate and state friction law (1) into a definition of  $\Theta(V, f)$ ,  
 358 2. differentiating (1) with respect to time and reorganizing it into a definition of  $\dot{V}(t)$ ,  
 359 and  
 360 3. substituting the definition of  $\Theta(V, f)$  and the definition of  $\dot{\Theta}$  that follows from the  
 361 aging law (2) into the definition of  $\dot{V}(t)$ ,

362 we arrive at the ordinary differential equation

$$363 \quad a \dot{V} = b r_0 [V^2 - V \Theta(V, f)^{-1}] + V \dot{f}, \quad (16a)$$

$$364 \quad \Theta(V, f)^{-1} := V^{\frac{a}{b}} \exp(-[f - f_0]/b) \quad (16b)$$

365  
 366 in which the friction coefficient  $f = f(\boldsymbol{\sigma}; \hat{t}, \hat{n})$  is treated as a property of – rather than  
 367 a constraint on – the stress tensor  $\boldsymbol{\sigma}$ .

368 By applying the same procedure to the proposed continuum friction and aging laws  
 369 (14) and (15) we obtain the analogous ODE for  $\gamma$ :

$$370 \quad a \dot{\gamma} = b r_0 [c_1 \gamma \mathcal{M}(\gamma) - c_2 \gamma \theta(\gamma, f)^{-1}] + \gamma \dot{f}, \quad (17a)$$

$$371 \quad \theta(\gamma, f)^{-1} := \gamma^{\frac{a}{b}} \exp(-[f - f_0]/b), \quad (17b)$$

372  
 373 in which  $f = f(\boldsymbol{\sigma})$  is given by the yield criterion (13) and  $\dot{f} = \dot{f}(\boldsymbol{\sigma}, \dot{\boldsymbol{\sigma}})$  is expressible  
 374 using the same yield criterion and the elastic constitutive equation (7).

375 Equations (16a,b) and (17a,b) are useful in mathematical and numerical analysis  
 376 of the problem because they eliminate a variable and an algebraic constraint, and at the  
 377 same time provide an ideal reference frame for establishing, and if necessary influenc-  
 378 ing, the ability of (17a,b) to reproduce the predictions made by (16a,b) in the sense of  
 379 the integral relation (6).

380 In the following derivation we will assume that the field of effective friction  $f(\vec{x})$ ,  $\vec{x} \in$   
 381  $\Omega$  in the neighborhood of a point  $\vec{x}_f$  on the fault is the same whether it is generated by  
 382 a hard or a soft discontinuity. This assumption ties into the principal assumption set out  
 383 in Section 2.2, which is revisited in Discussion section 5.5. Combining (16a,b), (17a,b),  
 384 and (6) leads to the following useful relation that describes the evolution of the anelas-  
 385 tic shear strain rate distribution over time:

$$386 \quad \dot{\varphi} \propto V [\lambda_0 c_1 \varphi \mathcal{M}(\varphi) - \varphi] - \Theta(V, f)^{-1} [\lambda_0^{\frac{a}{b}} c_2 \varphi^{1+\frac{a}{b}} - \varphi]. \quad (18)$$

387

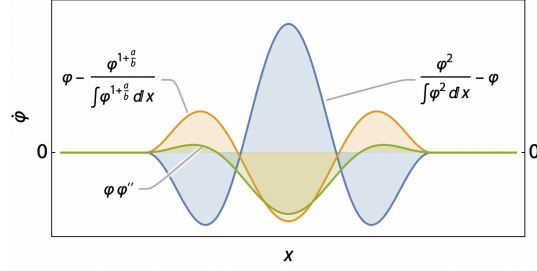


**Figure 3.** Influence of the different terms in Eq. (18) on the time derivative  $\dot{\varphi}$ . The first term (blue) can be seen to promote localization, while the second term (orange) favors the opposite. Finally the delocalizing influence of the nonlinear Laplacian term  $\varphi(x)\varphi''(x)$  is shown in green. The input function  $\varphi$  follows a cosine-squared distribution.

388 This differential equation tells us several things. Most importantly, for  $\gamma$  to remain in  
 389 accordance with  $V$  through the integral relation (6) over the transect  $T$ , the same in-  
 390 tegral of the left hand side of (18) must be zero. This requirement can only be met at  
 391 arbitrary  $(V, f)$  if both the term multiplied by  $V$  and the term multiplied by  $\Theta(V, f)^{-1}$   
 392 integrate to zero over  $T$ . This in turn can not in general be guaranteed unless

$$393 \quad c_1 := \mathcal{C}_1(\varphi) := \lambda_0^{-1} \left[ \int \varphi(x) \mathcal{M}(\varphi)(x) dx \right]^{-1}, \quad (19a)$$

$$394 \quad c_2 := \mathcal{C}_2(\varphi) := \lambda_0^{-\frac{a}{b}} \left[ \int \varphi(x)^{1+\frac{a}{b}} dx \right]^{-1}. \quad (19b)$$

396 We consider it undesirable for coefficients to depend in a time-dependent way on inte-  
 397 grals of the modeled quantities and therefore will be restricting our attention to specific  
 398 regimes of interest during which the values of the coefficients  $c_{1,2}$  can be predicted an-  
 399 alytically. We then employ those predicted values as model-specific constants in time and  
 400 space. We accept that this incurs a potential error whenever the state of the model is  
 401 outside the selected regime, and will critically evaluate this error using numerical mod-  
 402 els in Section 4.

403 Assuming the coefficients  $c_{1,2}$  have been chosen appropriately and for simplicity  
 404 that  $\mathcal{M}(\varphi) = \varphi$ , two additional observations can be made on the basis of (18):

- 405 1. The term that is multiplied by  $V$  promotes localization if  $\mathcal{M}(\varphi) = \varphi$  because  $\varphi^2$   
 406 is a narrower distribution than  $\varphi$  (Figure 3).

407 2. The opposite (delocalization; Figure 3) holds true for the term that is multiplied  
 408 by  $\Theta(V, f)^{-1}$  on account of the corresponding minus sign and the requirement that  
 409  $a, b > 0$ .

410 This localizing and delocalizing behavior is of great interest and will be treated in de-  
 411 tail in the following sections.

412 In the sections that follow we will assume to be operating on the fault-perpendicular  
 413 transect  $T$  and will denote with the scalar coordinate  $x$  the distance with respect to the  
 414 fault core, i.e.  $x = \hat{n}(\vec{x}) \cdot [\vec{x} - \vec{x}_f(\vec{x})]$ . This setting is in line with our assumption set  
 415 out in Section 2.2 that across-fault variations in anelastic strain rate are more compact  
 416 than its along-fault variations.

### 417 3.2 Runaway sliding and localization

418 Earthquakes occur as superexponential solutions to (16a,b). Prior to inertial damp-  
 419 ing the seismic slip rate  $V$  behaves as

$$420 \dot{V} \propto V^2.$$

422 This ODE has the solution

$$423 V(t) \propto \left(1 - \frac{t}{t_*}\right)^{-1}, \quad (20)$$

425 in which  $t_*$  is the time of the (hypothetical) singularity.

426 The same behavior occurs in (17a,b) in the limit

$$427 \dot{\gamma} \propto c_1 \gamma \mathcal{M}(\gamma), \quad (21)$$

429 and in (18) in the limit

$$430 \dot{\varphi} \propto V [\lambda_0 c_1 \varphi \mathcal{M}(\varphi) - \varphi].$$

431

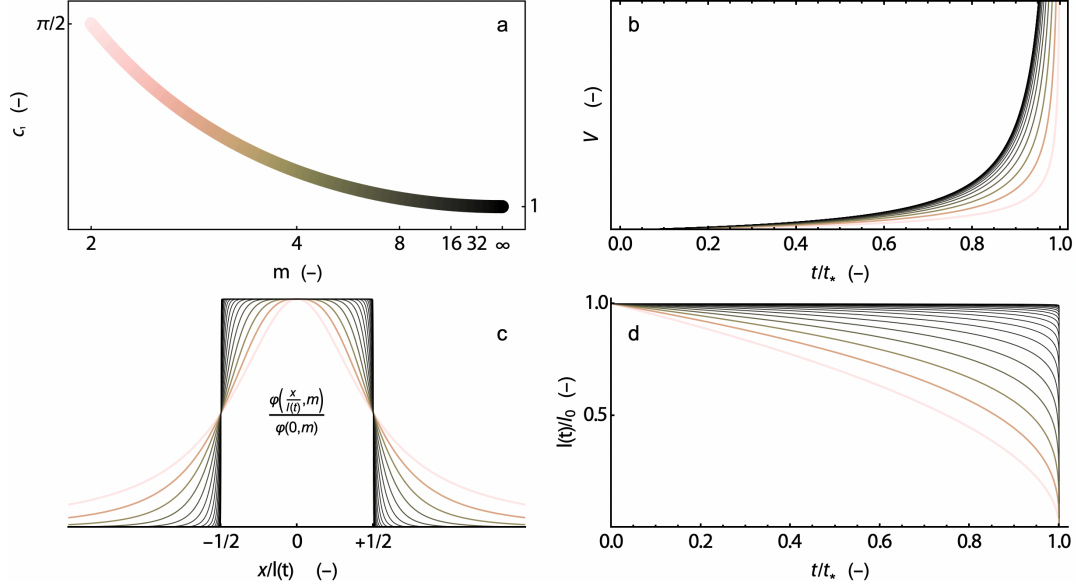


**Figure 4.** Asymptotic solutions during earthquake nucleation. a) Value of the dimensionless coefficient  $c_1(m)$  versus distribution exponent  $m$  (see main text) represented on a reciprocal axis that ranges between 2 and  $\infty$ . The thick line acts also as a color bar approximately indicating the value of  $m$  at which the individual lines in the remaining figures are plotted. b) Dimensionless slip rate  $V$  versus dimensionless time  $t/t_*$  to the slip rate asymptote for different values  $m \in \{2^{1.0}, 2^{1.5}, 2^{2.0} \dots\}$ . c) Nondimensionalized distributions  $\varphi(x/l(t); m)/\varphi(0; m)$  versus dimensionless coordinate  $x/l(t)$ . d) Dynamic dimensionless length scale  $l(t/t_*)/l_0$  versus dimensionless time  $t/t_*$ .

432 Assuming  $\mathcal{M}(\square) = \square$ , (21) can be shown to be solved by

$$433 \quad V(t) \propto \left(1 - \frac{t}{t_*}\right)^{m^{-1}-1}, \quad (22a)$$

$$434 \quad \varphi(t, x; m) := \left[ l(t)c_1(m) \left(1 + \left|\frac{2x}{l(t)}\right|^m\right) \right]^{-1}, \quad m \in \mathbb{R} \geq 2 \quad (22b)$$

$$435 \quad l(t) \propto V(t)^{(1-m)^{-1}}, \quad (22c)$$

$$436 \quad \gamma_0\gamma(t, x; m) := v_0V(t)\varphi(t, x; m), \quad (22d)$$

$$437 \quad c_1 = c_1(m) := \frac{\pi}{m} \csc \frac{\pi}{m}, \quad (22e)$$

439 in which the family of strain rate distributions  $\varphi(t, x; m)$  generated by the exponent  $m \in$   
 440  $\mathbb{R} \geq 2$  (Figure 4c) evolves in accordance with a time-variable characteristic width  $l(t)$   
 441 (Figure 4d). We note the following:

- 442 1. In the limit  $m \rightarrow \infty$ , the distribution  $\varphi(t, x; m \rightarrow \infty)$  reduces to a uniform dis-  
 443 tribution on the constant interval  $x \in [-l(0)/2, +l(0)/2]$ . The parameter  $c_1(m \rightarrow$   
 444  $\infty) = 1$  (Figure 4a) and the solution (22a) reduces to the interfacial solution (20).  
 445 However this limit also requires infinite mesh resolution or alternatively the def-  
 446 inition of two mesh discontinuities, which defeats our intent.
- 447 2. In the other end-member case where  $m = 2$ , the distribution  $\varphi(t, x; m = 2)$  is  
 448 known as the Cauchy distribution, and its characteristic width  $l(t) \propto V(t)^{-1}$ . The  
 449 parameter  $c_1$  is chosen in such a way that the distribution  $\varphi(t, x; m)$  integrates  
 450 to one and the time of the singularity matches the prediction of the interfacial model.  
 451 However, the trajectory of  $V$  towards the asymptote is unavoidably different (Fig-  
 452 ure 4b).
- 453 3. The functional form of  $\varphi(t, x; m)$  is not valid outside of the limiting case  $\dot{V} \propto V^2$   
 454 and is thus not stable over time, nor can it be enforced. Anelastic strain rate dis-  
 455 tributions that spontaneously establish over time in higher-dimensional simula-  
 456 tions are expected to be of approximate Cauchy type (low exponent  $m$ ) rather than  
 457 of uniform type (high exponent  $m$ ).

458 We therefore come to the qualitative conclusion that orders-of-magnitude increases of  
 459 slip rate correspond to orders-of-magnitude increase of strain rate locality, placing in-  
 460 surmountable demands on mesh resolution. If left unconstrained, this process culminates

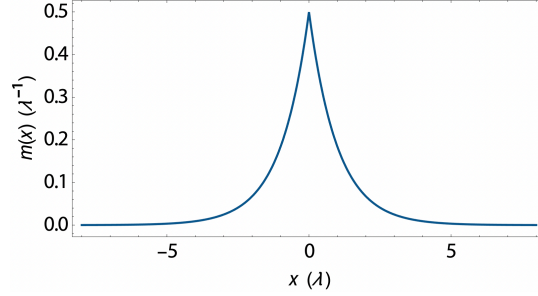


**Figure 5.** Plot of the mollifier  $m(x) = \frac{1}{2\lambda} \exp(-|\frac{x}{\lambda}|)$ .

461 in finite time to an infinite slip rate concentrated in an infinitesimally thin region of space  
 462 – a plane.

### 463 3.3 Non-local equivalent strain rate

464 In order to counter this tendency towards complete localization to a plane we in-  
 465 troduce the *non-local* operator  $\mathcal{M}$ , which *mollifies* its operand by means of convolution  
 466 with the symmetric distribution  $m(x)$ :

$$467 \mathcal{M}(\gamma)(t, x) := \int_T m(\xi) \gamma(t, x - \xi) d\xi. \quad (23)$$

469 We note that  $\mathcal{M}(\gamma)(t, x)$  still satisfies the relation (6) given that the distribution  $m$  in-  
 470 tegrates to unity over its domain.

471 Evaluation of  $\mathcal{M}(\gamma)$  requires the evaluation of the integral of  $\gamma$  over finite regions  
 472 of space and therefore lacks the mathematical locality that is desirable for continuum  
 473 models. We follow Peerlings et al. (1996) in constructing and truncating a Taylor series  
 474 linearization of (23). We find that a mollifier  $m(x) = \frac{1}{2\lambda} \exp(-|\frac{x}{\lambda}|)$  (Figure 5) leads  
 475 to series coefficients that are even powers of the length scale  $\lambda$ :

$$476 \mathcal{M}(\gamma)(t, x) = \sum_{n=0}^{\infty} \lambda^{2n} \partial_x^{2n} \gamma$$

478 This infinite sum can be rolled up into a recursive or *implicit* definition of  $\mathcal{M} = \mathcal{M}_{\text{im}}$

$$479 \mathcal{M}_{\text{im}}^{-1}(\tilde{\gamma}) := \tilde{\gamma} - \lambda^2 \partial_x^2 \tilde{\gamma}, \quad (24)$$

481 which is to be solved for the auxiliary variable  $\tilde{\gamma} = \mathcal{M}_{\text{im}}(\gamma)$ . Alternatively, the terms  
 482 beyond  $n = 1$  can be dropped, leading to the *explicit* definition of  $\mathcal{M} = \mathcal{M}_{\text{ex}}$

$$483 \mathcal{M}_{\text{ex}}(\gamma) := \gamma + \lambda^2 \partial_x^2 \gamma. \quad (25)$$

484

485 We note that any truncation of the Taylor series into a linear combination of even deriva-  
 486 tives of  $\gamma$  adheres to the integral property expressed in (6), even if these truncations lose  
 487 correspondence to a concrete mollifier. The implicit definition (24) has numerically ad-  
 488 vantageous properties (Peerlings et al., 1996), but requires the potentially costly solu-  
 489 tion of an elliptic PDE. For this reason we will use the explicit definition (25) in this work  
 490 and discuss the implicit definition (24) as an option for future implementations.

491 We generalize the second partial derivatives  $\partial_x^2$  with respect to the  $x$  coordinate  
 492 that appear in (24) and (25) to Laplacians  $\nabla^2$  in 3D, again assuming that variations of  
 493 strain rate across the fault are much bigger than variations along it.

### 494 3.4 Non-locality as a localization limiter

495 We repeat the analysis of Section 3.2, but now use the explicit non-local operator  
 496  $\mathcal{M}_{\text{ex}}$  in

$$497 \dot{\gamma} \propto c_1 \gamma \mathcal{M}_{\text{ex}}(\gamma)$$

499 and

$$500 \dot{\varphi} \propto V [\lambda_0 c_1 \varphi \mathcal{M}_{\text{ex}}(\varphi) - \varphi]. \quad (26)$$

502 We find that it is solved by

$$503 V(t) \propto \left(1 - \frac{t}{t_*}\right)^{-1}, \quad (27a)$$

$$504 \varphi(x) := \begin{cases} \frac{1}{\pi\lambda} \cos^2\left(\frac{1}{2}\frac{x}{\lambda}\right) & \forall x \in [-\pi\lambda, +\pi\lambda] \\ 0 & \forall x \notin [-\pi\lambda, +\pi\lambda] \end{cases}, \quad (27b)$$

$$505 \gamma_0 \gamma(t, x) := v_0 V(t) \varphi(x), \quad (27c)$$

$$506 c_1 := 2\pi, \quad \lambda_0 = \lambda, \quad (27d)$$

508 and observe that

- 509 1. The trajectory of  $V$  towards its asymptote can be made to exactly match the pre-  
 510 diction (20) of the interfacial rate and state friction formulation (16a,b) by a suit-  
 511 able choice of the constant  $c_1$ .

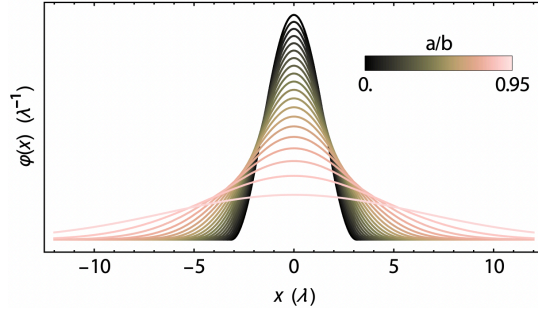


**Figure 6.** Steady-state distributions  $\varphi$  [cf. Eq. (29a)] of strain rate at various  $a/b$  versus distance  $x$  with respect to the fault core. The curve plotted for  $a/b = 0$  also corresponds to the most extreme strain rate localization at any value of  $a/b$  (see main text).

512        2. The cosine-squared distribution with prescribed size  $\lambda$  is an attractive steady state  
 513        during the process of earthquake nucleation. Further localization will not spon-  
 514        taneously occur. We interpret this distribution as striking a balance between the  
 515        localizing tendency of “ $\varphi^2 - \varphi$ ” and the delocalizing tendency of “ $\varphi \nabla^2 \varphi - \varphi$ ”  
 516        (Equation (18) and Figure 3).

517        The implicit non-local operator  $\mathcal{M}_{\text{ex}}$  in the same context does not have solutions  
 518        that simultaneously satisfy  $\dot{V} \propto V^2$  and  $\dot{\varphi} = 0$  with non-degenerate distribution  $\varphi =$   
 519         $\varphi(x/\lambda)$ .

### 520        3.5 Steady-state friction and deformation

521        As mentioned in Section 1.1, an important property of the state evolution law is  
 522        the steady state  $\Theta V = 1$ . We wish to retain this steady state in the continuum equiv-  
 523        alent (15) of the state evolution law, ideally at a steady strain rate distribution  $\varphi(x)$ , cf.  
 524        (18). We are thus interested in a steady-state solution to

$$525 \quad \dot{\varphi} \propto \lambda_0 c_1 \varphi \mathcal{M}_{\text{ex}}(\varphi) - \lambda_0^{\frac{a}{b}} c_2 \varphi^{1+\frac{a}{b}}, \quad (28)$$

526

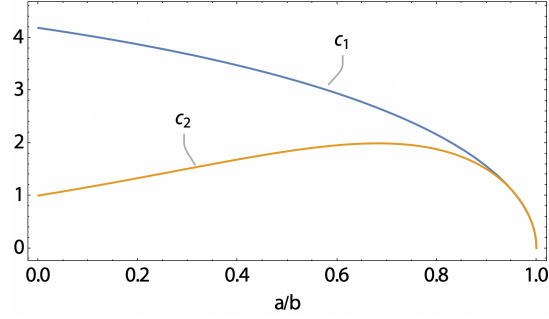


**Figure 7.** The coefficients  $c_1(\frac{a}{b})$  and  $c_2(\frac{a}{b})$ , given by Eq. (30a) and (30b), are plotted versus the acceptable range of  $\frac{a}{b}$ .

527 which exists as long as  $a, b > 0$  (standard requirements) and  $a < b$  (a net weakening  
528 fault), and reads

$$529 \quad \varphi\left(x; \frac{a}{b}\right) = \begin{cases} c_3\left(\frac{a}{b}\right) \frac{1}{\pi\lambda} \left[\cos\left(\frac{1}{2}\frac{x}{\lambda}\right)\right]^{2\left[1-\frac{a}{b}\right]^{-1}} & \forall x \in [-\pi\lambda, +\pi\lambda] \\ 0 & \forall x \notin [-\pi\lambda, +\pi\lambda] \end{cases} \quad (29a)$$

$$530 \quad \lambda := \lambda_0 \left[1 - \frac{a}{b}\right]^{-1}. \quad (29b)$$

532 Faults that are net strengthening or neutral ( $a > b$ ) do not possess a steady state of  
533 the strain rate distribution, instead delocalizing indefinitely.

534 The coefficients  $c_1$  and  $c_2$ , and the newly introduced  $c_3$ , are given by

$$535 \quad c_1\left(\frac{a}{b}\right) = \frac{1}{2}\pi^{\frac{3}{2}} \frac{\Gamma\left(1 + 2\left[1 - \frac{a}{b}\right]^{-1}\right)}{\Gamma\left(\frac{1}{2} + 2\left[1 - \frac{a}{b}\right]^{-1}\right)} c_3\left(\frac{a}{b}\right)^{-2} \quad (30a)$$

$$536 \quad c_2\left(\frac{a}{b}\right) = \frac{1}{2}\pi^{\frac{1}{2} + \frac{a}{b}} \frac{\Gamma\left(2\left[1 - \frac{a}{b}\right]^{-1}\right)}{\Gamma\left(\frac{1}{2}\left[3 + \frac{a}{b}\right]\left[1 - \frac{a}{b}\right]^{-1}\right)} c_3\left(\frac{a}{b}\right)^{-1 - \frac{a}{b}} \quad (30b)$$

$$537 \quad c_3\left(\frac{a}{b}\right) = \frac{1}{2}\pi^{\frac{1}{2}} \frac{\Gamma\left(1 + \left[1 - \frac{a}{b}\right]^{-1}\right)}{\Gamma\left(\frac{1}{2} + \left[1 - \frac{a}{b}\right]^{-1}\right)}, \quad (30c)$$

539 with  $\Gamma$  the gamma function that has the property  $\Gamma(n) = (n-1)!\forall n \in \mathbb{N}^+$ . The coef-  
540 ficients  $c_1$  and  $c_2$  are plotted as functions of  $a/b$  in Figure 7. The solutions (29a) are plot-  
541 ted in Figure 6, in which we can see that steady-state anelastic strain rate distributions  
542 have finite width and are therefore numerically resolvable as long as the aforementioned  
543 requirements on  $a$ ,  $b$ , and  $a/b$  are met.

### 3.6 Radiation damping

Finite time blow-up of the solution (Section 3.5) under quasi-static loading conditions is understood to be the consequence of the model's inability to radiate or dissipate liberated potential strain energy away from the fault. In what's called the *quasi-dynamic* or *radiation damping* approximation (Rice, 1993), a simple Newtonian sliding viscosity equal to half the material's shear impedance, here nondimensionalized as  $\eta = \frac{1}{2} \frac{\mu}{\sigma} \frac{v_0}{c_s}$ , is added to the friction law:

$$f = f_0 + a \log V + b \log \Theta + \eta V. \quad (31)$$

with  $c_s = \sqrt{\mu/\rho}$  the shear wave speed and in turn  $\mu$  the shear modulus and  $\rho$  the mass density.

We have no good way of replicating the behavior of the radiation damping term in the continuum model because introducing a term  $\propto c_3 \lambda_0 \eta \gamma$  into the yield function changes the structure of (17a,b) to such an extent that in the high strain rate limit it no longer admits non-degenerate steady-state or self-similar distributions of anelastic strain. Instead this bulk viscous analog to radiation damping can be shown to promote unconstrained delocalization that is only arrested after a sufficiently large friction drop. This means that no constant of proportionality  $c_3$  can be found that ensures a limit on slip rate to the extent that the term  $\eta V$  does. We choose  $c_3 = c_1$ , which seems to give good agreement of maximum slip rate between continuum and interfacial models, at least for the parameter values tested.

It may be preferable to think of the term  $\propto \eta \gamma$  as representing a residual viscosity (e.g. in extreme cases the viscosity of a melt) not subject to further weakening, and accept the limitation that the model with static momentum balance has a somewhat poorly constrained maximum slip rate.

The radiation-damped analog to the anelastic shear strain rate ODE (17a,b) is written for the newly introduced auxiliary field  $\zeta$ :

$$a \dot{\zeta}(t, x) = b r_0 (c_1 \mathcal{M}_{\text{ex}} \circ \gamma \circ \zeta(t, x) - c_2 \theta(\zeta, f)^{-1}) + \dot{f}(t), \quad (32a)$$

$$\theta(\zeta, f)^{-1} := (\gamma \circ \zeta(t, x))^{\frac{a}{b}} \exp\left(-\frac{1}{b} [f - f_0 - c_3 \eta \gamma \circ \zeta(t, x)]\right), \quad (32b)$$

$$\gamma(\zeta) := \frac{a}{c_3 \eta} W_0\left(\frac{c_3 \eta}{a} \exp \zeta\right), \quad (32c)$$

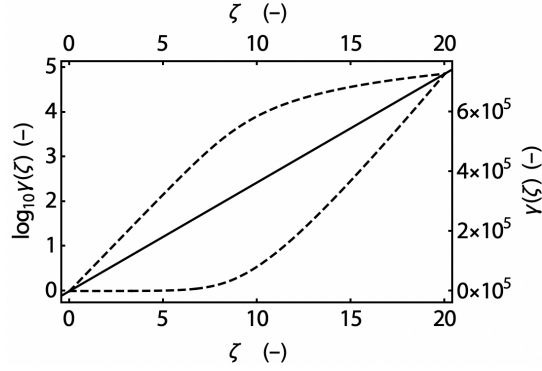


**Figure 8.** The function  $\gamma(\zeta)$  defined in Eq. (32c) plotted on a logarithmic scale in the top left diagonal portion of the figure and on a linear scale in the opposing portion, highlighting the exponential behavior of  $\gamma(\zeta)$  at low  $\zeta$  and the linear behavior at high  $\zeta$ .

575 with the principal branch  $W_0(f)$  of the Lambert W function, which is an implicit tran-  
 576 scendental function that is defined to be the solution to the equation  $W_0 \exp W_0 = f$ .  
 577 See Figure 8 for a plot of the relation (32c). While we acknowledge that the use of im-  
 578 plicit functions in physical descriptions is not ideal, from a practical standpoint there  
 579 is little problem because reliable and fast algorithms for computing the common Lambert  
 580 W function are included in many programming languages (Fritsch et al., 1973; Barry,  
 581 Barry, & Culligan-Hensley, 1995; Barry, Culligan-Hensley, & Barry, 1995; Johansson, 2020).

## 582 4 Numerical models

583 Analytical predictions made in preceding sections are complemented here with nu-  
 584 merical simulation results that better illustrate the complex time-dependent behavior  
 585 of the system of equations, and allow us to establish the consequences of approximations  
 586 and other model choices made in the process of formulating a local equivalent contin-  
 587 uum rate and state friction law. As before we restrict the scope to 1D models across the  
 588 shear band.

### 589 4.1 Equations

590 On the one-dimensional line  $x \in [-L/2, +L/2]$  that deforms under simple shear,  
 591 analogous to the transect  $T$  defined in Figure 1, we model the compact equation (32a,b)  
 592 together with the one-dimensional static momentum balance equation  $\partial\tau/\partial x = 0$  cf.

593 (8), elastic constitutive equation  $\dot{\tau}(t, x) = \mu [\partial v(t, x)/\partial x - 2\gamma_0\gamma(t, x)]$  cf. (7) (with  $\mu$   
 594 the shear modulus as before), yield equality  $\tau(t) = f(t)\sigma$ , and finally the boundary con-  
 595 ditions  $v(t, x = \mp L/2) = \mp V_p/2$  combined into the single ODE

$$596 \quad \dot{f}(t) = \frac{\mu}{\sigma} \left[ \frac{V_p}{L} - \frac{\mathcal{V}(\gamma \circ \zeta)}{L} \right], \quad (32d)$$

597  
 598 with  $V_p$  the ‘plate’ driving velocity that is applied antisymmetrically on both ends of the  
 599 domain. This equation uses (6) that relates slip velocity to the integral (from  $-L/2$  to  
 600  $+L/2$ ) of anelastic shear strain rate  $\gamma$ , as well as (32c) for the relation between  $\gamma$  and  
 601 the auxiliary field  $\zeta$ .

602 The system is closed with natural boundary conditions  $\partial\gamma/\partial x = 0$  on  $\gamma(t, x =$   
 603  $\mp L/2)$ , and initial conditions  $f(t = 0) = f_0 + \Delta f$  and  $\gamma(t = 0, x) \propto \varphi_0(x) + \epsilon$ , with  
 604  $\varphi_0(x)$  deriving from the analytical prediction (29a) and  $\epsilon$  a necessary but small homo-  
 605 geneous background value of anelastic shear strain rate. As long as this value is small  
 606 enough ( $\epsilon \ll V_p/L \ll v_0/L$ ) and the ‘tails’ of the strain rate distribution can be ig-  
 607 nored, the required computational domain size may be based on the length scale  $\lambda$  and  
 608 therefore cover only a potentially small fraction of the line  $[-L/2, +L/2]$ , greatly reduc-  
 609 ing the computational cost.

610 The solution procedure is outlined in Appendix Appendix A.

## 611 4.2 Continuum velocity stepping friction experiments

612 Velocity stepping laboratory experiments form the foundation on which rate and  
 613 state friction was proposed (Dieterich, 1978). We compare numerical velocity stepping  
 614 experiments of a traditional rate and state friction-governed interface with our proposed  
 615 continuum equivalent under the same conditions. We impose a driving velocity that fol-  
 616 lows a smooth square wave function with respect to sliding distance  $\delta$ :

$$617 \quad \log_{10}(V_p(\delta)/v_0) = \frac{2}{\pi} \tan^{-1} \left( -\frac{1}{\nu} \cos \left( \frac{\pi \delta}{n d_c} \right) \right), \quad (34)$$

618  
 619 with  $n = 20$  the amount of slip weakening distances  $d_c$  between velocity steps, and  $\nu =$   
 620  $10^{-3}$  a parameter that controls the smoothness of the smooth square wave, with small  
 621 numbers giving the squarest result (see Figure 9a). Some smoothness is important to main-  
 622 tain numerically stable results. The low and high driving velocities are  $10^{-1}v_0$  and  $10^{+1}v_0$   
 623 respectively. Other model parameters are given in Table 4.2. Inertial effects may be ig-  
 624 nored (both in the original lab experiments and in our simulations) due to the low driv-

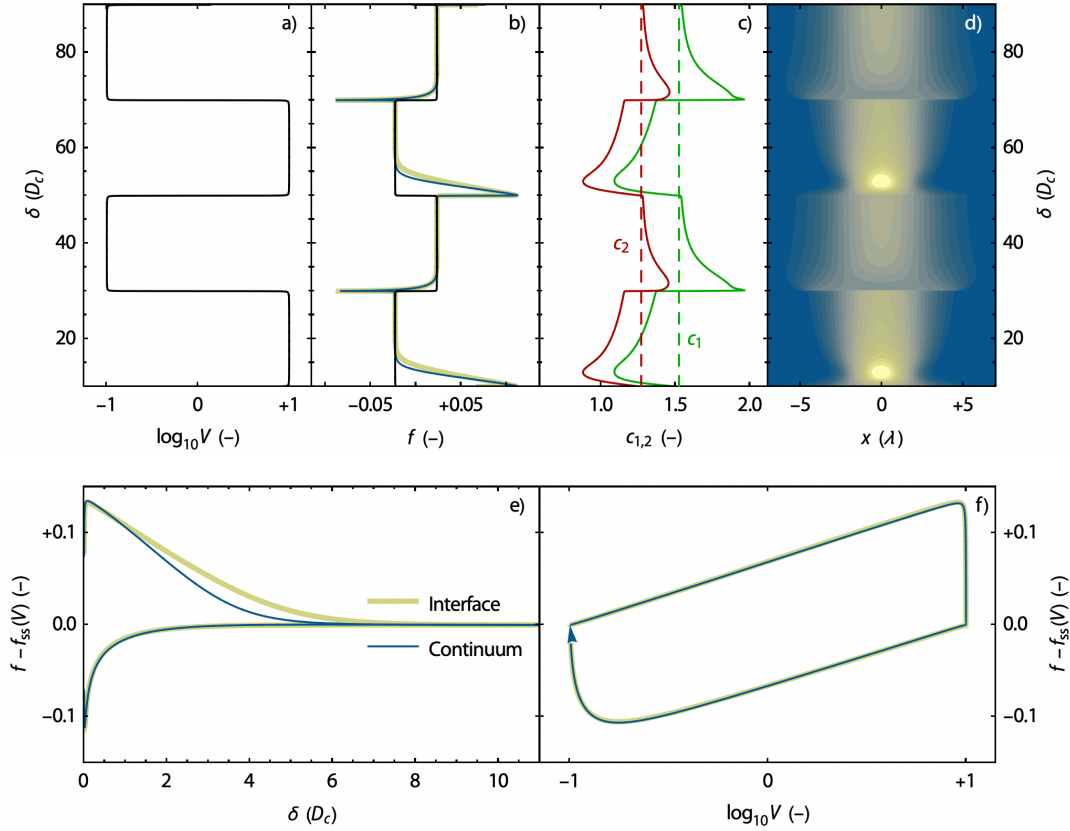


**Figure 9.** Results of the numerical velocity stepping experiments: a) dimensionless sliding velocity  $V$  closely tracking a smooth square wave signal (Eq. (34)); b) frictional response of the interfacial reference model (thick yellow line) and continuum model (dark blue line) with for reference the theoretical steady-state friction  $f_{ss}(V)$  (black line); c) measured (solid lines; cf. Eq. (19a,b)) vs. used (dashed lines; cf. Eq. (30a,b)) values of the dimensionless coefficients  $c_{1,2}$ ; d) distribution  $\varphi = \gamma/V$  of anelastic shear strain rate with darker blue colors reflecting very low values and bright yellow colors reflecting high values, and contours distributed evenly on a linear scale. Reflecting the ultimate slip-dependence (rather than direct time-dependence) of the rate and state friction laws, curves in panels a)–d) are plotted against sliding distance  $\delta$  (measured in critical slip distances  $d_c$ ) on the vertical axis. Panel e) shows an enhanced view of the evolution of the instantaneous friction coefficient towards the steady-state value with slip distance  $\delta$ , simultaneously showing a positive and negative step for both the interface and continuum models. Panel f) displays a full cycle of both models in terms of sliding velocity  $V$  and friction perturbation  $f - f_{ss}$ . It distinguishes interface and continuum models by line color and thickness as in panels b) and e).

**Table 1.** Parameter values used in the velocity stepping experiment

parameter	value	unit
$a$	$2 \cdot 10^{-2}$	1
$b$	$3 \cdot 10^{-2}$	1
$d_c$	$10^{-5}$	m
$v_0$	$10^{-6}$	$\text{m s}^{-1}$
$\rho$	$10^{+3}$	$\text{kg m}^{-3}$
$\mu$	$10^{+10}$	Pa
$c_s$	$3.162... \cdot 10^{+3}$	$\text{m s}^{-1}$
$\eta$	$1.581... \cdot 10^{-6}$	1
$\sigma$	$10^{+6}$	Pa
$d_c$	$5.00 \cdot 10^{-4}$	m
$\lambda$	$\sim 1.4 \cdot 10^{-4}$	m
$c_1$	$1.531...^{\text{a}}$	1
$c_2$	$1.276...^{\text{a}}$	1
$r_0$	$v_0/d_c$	$\text{s}^{-1}$
$\nu$	$10^{-3}$	1
$n$	20	1

Some rate and state parameter values are roughly based on Erickson et al. (2020).  
<sup>a</sup>Using (30a) and (30b) with stated values of  $a$  and  $b$ .

ing velocity. Thus, the radiation damping viscosity  $\eta$  is set to zero and its effects not discussed here. In the limit  $\eta \rightarrow 0^+$ , (32c) simply reduces to  $\gamma(\zeta) = \exp \zeta$  or equivalently  $\zeta(\gamma) = \ln \gamma$ , which reduces (32a,b) back to (17a,b).

Because the domain size  $L$  is very small and the system (32a–32d) therefore stiff, the friction tends to a stable steady state after being perturbed by a velocity step rather than developing a limit cycle. This also means that  $\mathcal{V}(\gamma) \approx V_p(\delta)$ . In fact,  $\mathcal{V}(\gamma)$  and  $V_p(\delta)$  are so close that their difference would not register in Figure 9a.

In the following, we use the terms time-dependence and slip dependence interchangeably but note that the rate of change of either is not constant from the perspective of the other. A slip-centric presentation of velocity-stepping results is commonplace in the earlier cited literature.

In Figure 9b (and its detailed view 9e) we explore the similarities and differences in slip dependence of the friction coefficient  $f$  between the interfacial and continuum velocity stepping experiments. Based on (18), we expect that a velocity step perturbs not just the magnitude of anelastic shear strain, but also its distribution (Figure 9d) and therefore the theoretical value of the dimensionless coefficients  $c_{1,2}$  (Section 3.3; Equations (19a) and (19b); Figure 9c, solid lines) away from steady state. Since these coefficients are actually set to their constant steady-state predictions (Section 3.5; Equations (30a) and (30b); dashed lines in Figure 9c), we expect some differences in time or slip dependence to occur. Notably, a positive velocity step leads to a temporary localization of anelastic deformation and a corresponding decrease in the theoretical values of  $c_{1,2}$  with respect to steady state. This leads to an overestimation of corresponding terms in the right-hand-side of (32a) and a faster decay towards the steady-state friction coefficient (Figure 9b,e) of the continuum model with respect to the interfacial model. A negative velocity step causes temporary delocalization (Figure 9d) and under-estimation of terms involving  $c_{1,2}$  in (32a), but does not lead to any noticeable difference in friction coefficient evolution towards the steady state between the two models (Figure 9b,e). We conclude that those terms involving  $c_{1,2}$  are negligible in this situation.

In Figure 9c and 9d it can also be seen that the *distribution* of anelastic shear strain rate tends more slowly to a steady state than the friction coefficient itself, and moreover that this decay is slower after a positive velocity step than after a negative one. In fact, the  $40 d_c$  wavelength we use for the input signal (34) is too small to enable a somewhat

657 complete evolution towards steady-state of the anelastic strain rate distribution during  
 658 the high-velocity regime, but we have taken care that this does not meaningfully impact  
 659 the results during the subsequent low-velocity regime.

660 Figure 9f shows that in  $V$ - $f$  phase space where time- or slip-dependence is hidden,  
 661 the response of the continuum and interface models are practically equivalent.

### 662 4.3 Continuum spring-slider experiments

663 Whereas velocity stepping experiments are useful for studying the way in which  
 664 friction can be attracted to a steady state, permanently out-of-equilibrium ‘limit cycle’  
 665 behavior is more interesting in the study of earthquake dynamics. We achieve this be-  
 666 havior by increasing the size of the domain and the distance of the boundary conditions  
 667 by many orders of magnitude ( $L = 80$  km) with respect to the velocity stepping ex-  
 668 periments. Thereby, we greatly reducing the effective stiffness of the medium as can be  
 669 seen in (32d). This is analogous to performing the so-called spring-slider experiment in  
 670 which a mass is dragged over a surface by a spring that is tensed at a constant rate to  
 671 give an educational example of the apparent stick-slip behavior of seismogenic faults. Our  
 672 goal in performing this experiment is to determine the degree to which the here proposed  
 673 continuum friction laws match the predictions made by Dieterich and Ruina’s interfa-  
 674 cial laws and to describe the transient behavior of anelastic strain rate in the added di-  
 675 mension. Radiation damping plays an essential role in these experiments to close the limit  
 676 cycle that otherwise extends to  $V \rightarrow \infty$  (Section 3.6). As discussed in the same sec-  
 677 tion, our continuum approximation to radiation damping precludes a steady-state anelas-  
 678 tic strain rate distribution at high slip velocity, a fact that directly contradicts one of  
 679 our precepts (Section 3.1). Therefore we anticipate a larger discrepancy between inter-  
 680 face and continuum models here than was observed during the velocity stepping exper-  
 681 iments.

682 Figure 10 depicts the evolution of quantities of interest over the course of multi-  
 683 ple orbits of the solution as it converges to the limit cycle. The first important obser-  
 684 vation is that the continuum model still appears to exhibit spontaneous limit cycle be-  
 685 havior. Due to the appropriately chosen initial condition, the wind-up period is short  
 686 and there is little variability between successive revolutions. As predicted (Section 3.5),  
 687 the nucleation phase is marked by runaway amplitude increase of a quasi-steady strain

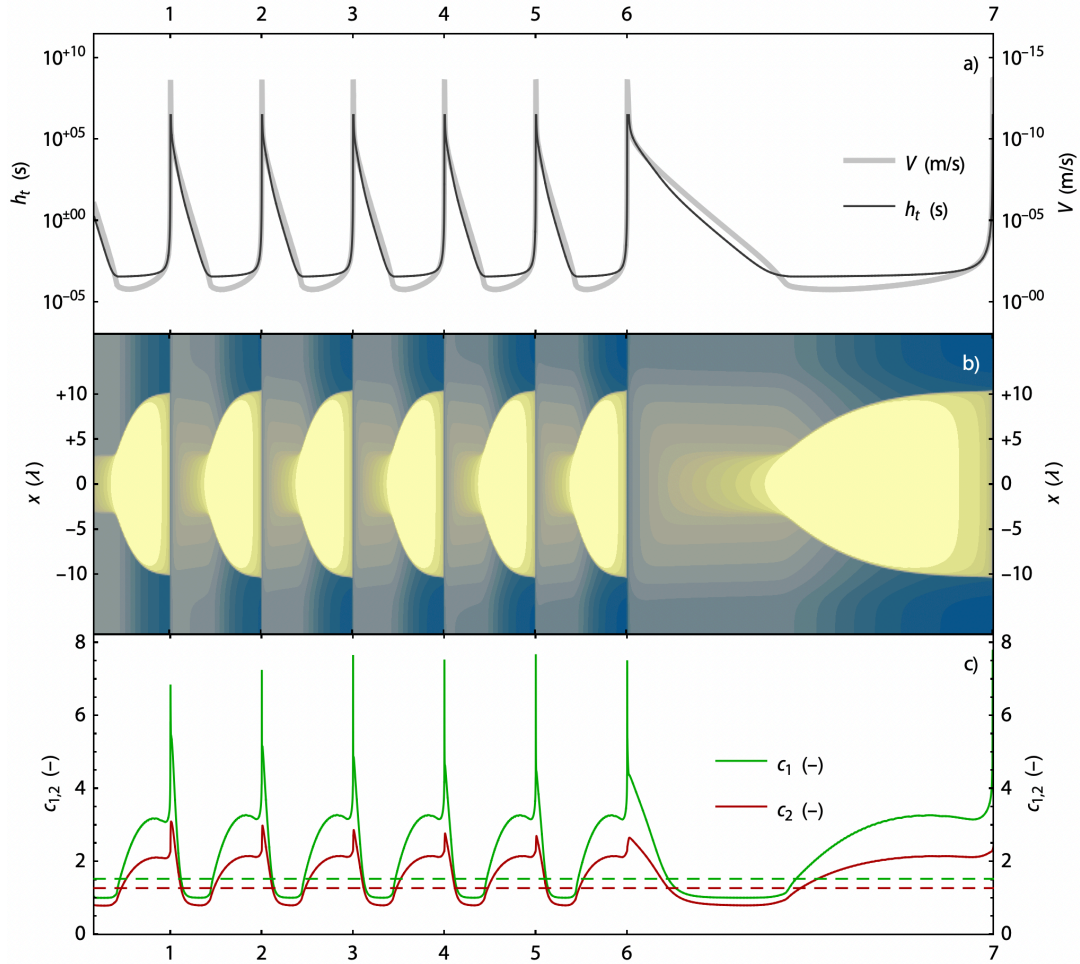


**Figure 10.** Evolution of the continuum seismic cycle simulation demonstrated by a succession of six events plotted against time step count on the horizontal axis, with a seventh event stretched by a factor four in order to better show some features of an individual event. The end of each event is punctuated by a slip velocity minimum and numbered 1 to 7 on the horizontal axes. Each revolution around the limit cycle takes 83.00 years and 107,500 time steps to complete. Panel a: time step size  $h_t$  (thin dark line; left axis; logarithmic scale) and slip velocity  $V$  (thick bright line, right axis; logarithmic scale). The former serves to aid the interpretation of the time-dependent progression of each event while the latter gives a sense of magnitude to the color scale of panel b. Axes are chosen so that together these curves express the imperfect reciprocal relation between time step and slip velocity. Panel b: logarithm of dimensionless anelastic shear strain rate versus signed distance  $x$  measured in number of length scales  $\lambda$  away from the shear zone center. Bright yellow colors indicate high strain rate; dark blue colors indicate low strain rate. Contours are drawn at equal intervals in log space. No explicit color scale is given because the magnitude of anelastic shear strain rate  $\gamma$  is tied to the value of  $\lambda$  in order to produce a length-scale independent history of sliding velocity  $V$  (panel a). Panel c: measured (solid lines; cf. Eq. (19a,b)) vs. used (dashed lines; cf. Eq. (30a,b)) values of the dimensionless parameters  $c_{1,2}$ .

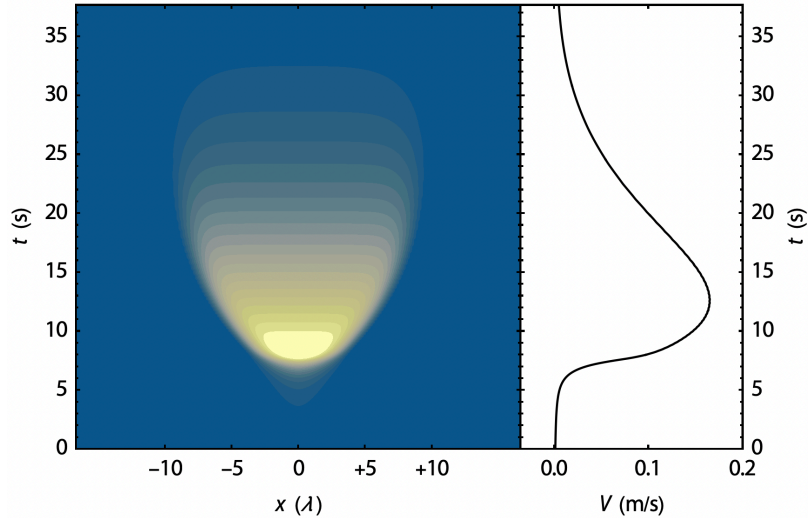


**Figure 11.** Focus on the last event of Figure 10, here visualized in panel a by strain rate on a linear color and contour scale and in panel b by slip rate  $V$ , both versus a linear time scale in seconds.

688 rate distribution (panel b). As before, we measure the dynamic value of the coefficients  
 689  $c_{1,2}$  from the strain rate distribution following (19a,b), and compare to the analytically  
 690 derived steady-state values (30a,b). In line with analytical predictions this phase is also  
 691 accompanied by measured values of  $c_{1,2}$  (panel c) that are slightly lower than the con-  
 692 stant values that are prescribed (dashed lines in panel c). The opposite situation occurs  
 693 throughout the remainder of each cycle where anelastic strain is more widely distributed.  
 694 We can attribute this directly to the effect of ‘radiation damping’ or residual viscosity,  
 695 which exerts a delocalizing influence. Figure 11 provides a more intuitive view of the short-  
 696 lived delocalizing behavior of a strain pulse using linear rather than logarithmic scales.  
 697 We emphasize that the ultimate extent of coseismic delocalization compared to the length  
 698 scale  $\lambda$  is dependent on model and material parameters, among which the effective stiff-  
 699 ness of the medium.

700 Large peaks in the measured values of  $c_{1,2}$  shown in panel c of Figure 10 occur dur-  
 701 ing the post- and interseismic phase, where anelastic shear strain rate is broadly and quite  
 702 uniformly distributed. The values that are actually used (dashed lines) are way too small  
 703 here, however, terms that do not involve these coefficients dominate the time-dependent  
 704 behavior in this regime and the discrepancy’s consequences are limited. This is largely  
 705 confirmed in Figure 12, which tabulates the evolving scalar properties of a limit cycle

706 of the interfacial and continuum models of rate and state friction. In particular, the du-  
 707 ration of the limit cycle (first column, panels a–c, time in years on the horizontal axis)  
 708 is very similar even though the timing of the event in relation to its enclosing slip ve-  
 709 locity minima is somewhat different.

710 Markedly different are the coseismic aspects of the limit cycle. Panel e of the mid-  
 711 dle column and panels h–j of the right column of Figure 12 clearly show this. The con-  
 712 tinuum model has a faster stress drop (panel h,  $U' \propto f$ ) and a more symmetric slip rate  
 713 response with time compared to the interfacial model. The limit cycle depicted in lin-  
 714 ear phase space  $(U', V)$  in Figure 12e shows a skewed triangular trajectory of the inter-  
 715 facial model and a more parabolic trajectory for the continuum model. It appears that  
 716 the amount of stress drop that happens *before* peak slip rate in the interfacial model is  
 717 small – about 10% of the total stress drop. At the same point in the continuum model  
 718 the stress drop is already about one third of the total. The same limit cycle shown in  
 719 Figure 12f in log-linear phase space  $(U', \log_{10} V)$  allows us to see that there are subtle  
 720 differences between the limit cycles of the interfacial and continuum models over the whole  
 721 range of slip velocities.

722 A further result of practical interest is the difference in adaptively chosen time step  
 723 between the interfacial and continuum models. Figure 10a shows an approximate inverse  
 724 relation between the time step of continuum model to the aggregate slip velocity  $v_0 V$ ,  
 725 which is unsurprising seeing how  $d_c/[v_0 V(t)]$  gives a sensible local time scale for both  
 726 interfacial and continuum rate and state friction models. The approximate inverse re-  
 727 lation breaks down at large time scales where the corresponding time steps are truncated  
 728 to a fixed value of 0.1 yr, and at large slip velocity and small time step, where the time  
 729 scale of the continuum model becomes dominated by large spatial gradients and is gen-  
 730 erally much smaller than that of the interfacial model (Figures 12d,g,k). From these same  
 731 plots it can be seen that, just like stress begins to drop in significant advance of an event,  
 732 so too does the time step of the continuum model.

733 Finally, we remark that spatial resolution tests indicate that the quality of the so-  
 734 lution is only influenced by the ratio of cell size  $h_x$  to  $\lambda$ , with acceptable results achieved  
 735 when  $h_x/\lambda \geq 10$ . For the results presented here we have used  $h_x/\lambda = 20$ . Changing  
 736  $\lambda$  in proportion to  $h_x$  does nothing except to cause a wider or narrower but equally well  
 737 resolved strain distribution and a virtually identical limit cycle.

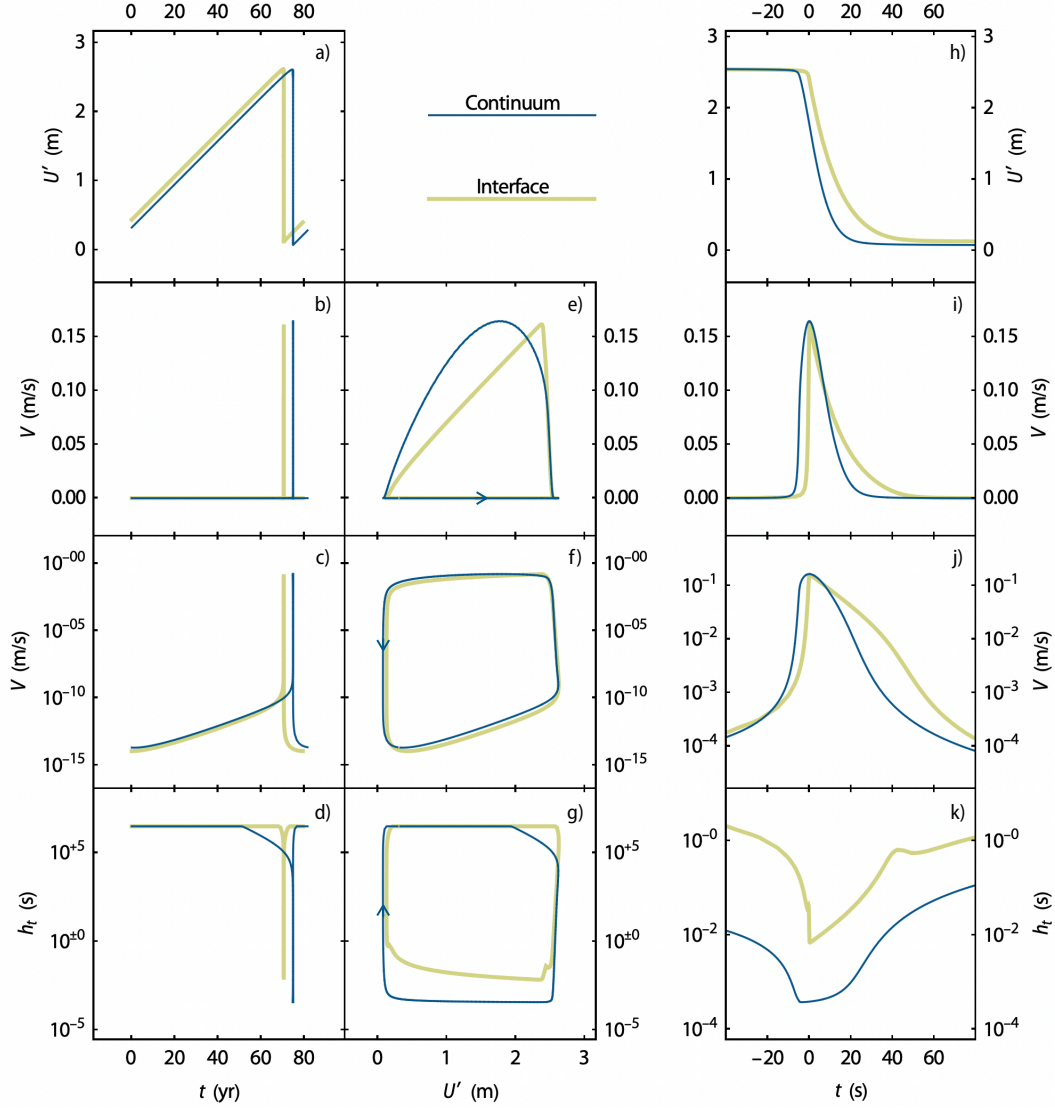


**Figure 12.** Panels a–g: behavior of the interfacial (bright yellow lines) and continuum (dark blue lines) models for a full limit cycle. Panels h–k: focus on the 100 seconds around an event. From left to right, horizontal axes are: time  $t$  in years, slip deficit  $U'$  in meters (linearly related to shear stress  $\tau$  and friction coefficient  $f$ ), and time  $t$  in seconds. Vertical axes from top to bottom are slip deficit  $U'$  in meters, slip velocity  $V$  in meters per second on a linear scale, the same on a logarithmic scale, and finally the time step size  $h_t$  in seconds on a logarithmic scale. Where limit cycles are shown (middle column, panels e–g), the cycle sense is indicated with small arrows.

## 5 Discussion

So far we have argued for a visco-elastic continuum rheology that resembles both the mathematical presentation as well as the resulting behavior of traditional interfacial rate and state friction as described by Dieterich and Ruina in their respective seminal publications. Before addressing this work in the context of a much broader body of existing research and reflecting on critical assumptions made in this work and its extension towards the future, we briefly touch upon some alternate branches of our proposed theory that have been left out so far for the sake of clarity.

### 5.1 A primitive reformulation

In contrast to traditional models of plasticity, the continuum rate and state friction laws presented here possess a continuous time-dependence that makes the anelastic shear strain rate  $\gamma$  a predictable quantity rather than one that is to be solved by a constrained optimization algorithm (e.g. Simo & Taylor, 1985; Duretz et al., 2018). This is apparent from the ODE (17a,b) for  $\gamma$ , but is hidden in the Dieterich-Ruina form (14) and (15) of the continuum rate and state friction rheology. However, (17a,b) lacks the simplicity and elegance of the Dieterich-Ruina system and is difficult to interpret as the resultant of physical phenomena. By defining a set of primitive variables  $\kappa$  and  $\psi$  as

$$\dot{\kappa} = r_{\kappa} \gamma \quad (35)$$

$$\dot{\psi} = r_{\psi} \gamma^{a/b} \exp(-[f(\boldsymbol{\sigma}) - f_0]/b),$$

with the respective reference rates  $r_{\kappa} = r_0 c_1$  and  $r_{\psi} = r_0 c_2$ , we are able to write a more expressive formulation of (17a,b) as

$$\dot{\kappa} = r_{\kappa} \gamma = r_{\kappa} \left( \dot{\psi} / r_{\psi} \right)^{\frac{b}{a}} \exp([f(\boldsymbol{\sigma}) - f_0]/a) \quad (36)$$

$$\dot{\psi} = r_{\psi} \exp(\mathcal{M}_{\text{ex}}(\kappa) - \psi), \quad (37)$$

that still closes the momentum balance equation (8) and elasto-plastic constitutive equation (7) without algebraic constraints and thus without requiring a constrained optimization algorithm. Equation (37) can accommodate radiation damping using the Lambert W function analogous to the way it was discussed in Section 3.6.

We recognize  $\kappa(t, x)$  as a dimensionless measure of accumulated anelastic shear strain and therefore assign to  $\psi$  the meaning of a ‘virtual’ or ‘unrealized’ strain. In spite of the

769 conceptual appeal of (36) and (37), it can be difficult to choose appropriate initial con-  
 770 ditions for  $\psi$ .

## 771 5.2 Quadratic diffusion

772 Instead of the mollified term  $\gamma \mathcal{M}(\gamma)$  that was introduced in (15) and used through-  
 773 out the remainder of this work, we could have chosen to use  $\mathcal{M}(\gamma^2)$ :

$$774 \quad a \dot{\gamma}_l = b r_0 [c_1 \mathcal{M}(\gamma^2) - c_2 \gamma \theta(\gamma, f)^{-1}] + \gamma \dot{f}. \quad (38)$$

776 and the definition of  $c_1$  is adapted to the new way of mollifying according to the same  
 777 principles as laid out in Section 3.

778 This choice has advantages and disadvantages. A major disadvantage is that it does  
 779 not seem to allow a return from (38) to the more elegant Dieterich-Ruina form (14) and  
 780 (15), nor to the compact form (36)–(37) proposed in the preceding section. A clear ad-  
 781 vantage is that, taken together with the explicit non-local operator  $\mathcal{M}_{\text{ex}}$ , (38) produces  
 782 a degenerate reaction-diffusion equation of generalized Fisher or Kolmogorov–Petrovsky–Piskunov  
 783 (KPP) type (Fisher, 1937; Kolmogorov et al., 1937) that remains well-posed at and around  
 784  $\gamma = 0$ . This leads to shear zone solutions that can propagate into perfectly intact rock  
 785 without taking recourse to an arbitrary small initial condition on  $\gamma$ . Furthermore, un-  
 786 der quadratic diffusion, the function  $\gamma(\zeta)$  used in the ODE form (32a–d) in Section 3.6  
 787 becomes algebraic instead of transcendently implicit.

788 We have reproduced all results presented in Section 4 with this quadratic diffusion  
 789 term and zero background anelastic strain rate too, and observe numerically smoother  
 790 and better resolved shear fronts during the coseismic delocalization phase. These fronts  
 791 also travel faster and further than in the linear diffusion case leading to a larger discrep-  
 792 ancy between measured and used values of the coefficients  $c_{1,2}$  and consequently larger  
 793 deviations of the limit cycle with respect to that of the interfacial rate and state friction  
 794 model. The generalized Fisher–KPP type equation has merited a large body of theoret-  
 795 ical research (e.g. Sánchez-Garduño & Maini, 1994, 1995, 1997; Sherratt & Marchant,  
 796 1996; S. Petrovskii & Li, 2003; S. V. Petrovskii & Li, 2006; Gilding & Kersner, 2005; Y. Wu  
 797 et al., 2006; Y. Li & Wu, 2008; Malaguti & Ruggerini, 2010; Broadbridge & Bradshaw-  
 798 Hajek, 2016) and therefore some of the above mentioned empirical findings may be given  
 799 a theoretical underpinning in future work.

### 5.3 Relation to regularized damage or plasticity models

As shown in Section 4.3 there are circumstances under which the transient viscous rheology proposed in this work promotes a spontaneous organization of periods and regions of negligible anelastic strain rate and those of significant anelastic strain rate. Even though a critical yield stress seems to be an emergent rather than an inherent property of the system of equations and initial and boundary conditions, it is tempting to think of this rheology as a smooth plasticity model.

We have shown (Section 3.5) that our model requires regularization by a non-local strain rate measure to avoid spurious mesh dependence. Non-locality in one form or another has been applied to combat ill-posedness in e.g. Bažant et al. (1984); Triantafyllidis and Aifantis (1986); Schreyer and Chen (1986); Pijaudier-Cabot and Bažant (1987); de Borst and Mühlhaus (1992); Peerlings et al. (1996); Jirásek (1998); Bažant and Jirásek (2002); Engelen et al. (2003); Jirásek and Rolshoven (2009b, 2009a); Burghardt et al. (2012); Lyakhovskiy et al. (2011); Lyakhovskiy and Ben-Zion (2014b, 2014a); Lyakhovskiy et al. (2016); Kurzon et al. (2019, 2020); Kiefer et al. (2018); Abdallah et al. (2020).

The comprehensive non-local damage-breakage rheology of Lyakhovskiy et al. (2011); Lyakhovskiy and Ben-Zion (2014b, 2014a); Lyakhovskiy et al. (2016), firmly rooted in thermodynamic theory and well-calibrated to match observations, is one of few damage theories developed to cover the full process of earthquake generation and healing (Lyakhovskiy et al., 2016; Kurzon et al., 2019, 2020). As in our model, the nonlocality in theirs is of Gradient type, but differs subtly in that it acts on the damage parameter rather than on the anelastic shear strain rate. Another example is the Godunov-Peshkov-Romenski model (S. Godunov & Romenskii, 1972; S. K. Godunov & Romenskii, 2003; Resnyansky et al., 2003; Romenskii, 2007; Romenski et al., 2020), which was first used in Gabriel et al. (2021) to simulate dynamic rupture and off-fault damage generation. This model differs from our model and the aforementioned damage-breakage rheology in a fundamental way in that shear bands are produced by damage waves described by hyperbolic equations rather than parabolic equations of reaction-diffusion type.

Our model differs from phase-field models of fracture in some respects. By allowing the spatial distribution of anelastic shear strain rate to vary over time, we are unable to retrieve a phase field  $d \in (0, 1)$ . We do not consider this a disadvantage, but do acknowledge that this is mainly a consequence of our viscous approximation to ra-

832 diation damping (Section 3.6), which gives rise to a reaction term in (32) that can be  
 833 considered as the derivative of a double-well potential. Multiple authors have commented  
 834 critically on the use of double-well potentials in phase field methods (e.g. Kuhn et al.,  
 835 2015; J.-Y. Wu, 2017).

836 Interestingly, our bulk viscous analog of radiation damping also appears as a reg-  
 837 ularization technique in some plasticity models (Needleman, 1988; Peirce et al., 1983;  
 838 Duretz et al., 2019, 2020, 2021; de Borst & Duretz, 2020; Stathas & Stefanou, 2022). In  
 839 these models the Kelvin–Voigt arrangement of yield strength and Newtonian viscosity  
 840 truncates the steady-state anelastic strain rate that may be achieved, forcing a shear zone  
 841 to have a finite width in order to slide at a certain macroscopic rate. In our model, the  
 842 same viscosity also introduces an effective upper bound on anelastic strain rate attained  
 843 during the limit cycle and causes subsequent delocalization, but we must still rely on the  
 844 gradient regularization to combat the unbounded localization that would otherwise hap-  
 845 pen even at low strain rate. A detailed analysis of the efficacy of viscous regularization  
 846 in dynamic problems is made in Stathas and Stefanou (2022).

#### 847 **5.4 Relation to other transient continuum rheologies**

848 The framework here proposed can be seen as a generalization of the work of Herrendörfer  
 849 et al. (2018); Preuss et al. (2019, 2020), who made the purely local substitution  $v_0 V \rightarrow$   
 850  $h_x \gamma_0 \gamma$  and used a Drucker-Prager elastoplastic model similar to the one set out in Sec-  
 851 tion 2.4. Setting  $\lambda, \eta = 0$  and assuming that strain rate fully localizes into a discrete  
 852 Dirac function sampled every  $h_x$ , we find that the coefficients  $c_1$  and  $c_2$  become  $h_x/d_c$   
 853 and 1 respectively, substitution of which into (15) yields Herrendörfer’s version of the  
 854 aging law. Their model was first applied along a predefined staggered grid line in Herrendörfer  
 855 et al. (2018), obeying the discrete Dirac distribution of anelastic shear strain automat-  
 856 ically and effectively yielding a numerical method analogous to the stress glut method  
 857 of Andrews (1999). Herrendörfer’s model was subsequently applied in an unconstrained  
 858 evolving continuum model in Preuss et al. (2019, 2020), but notwithstanding measures  
 859 put in place that acknowledge the changing distribution of shear strain rate within a shear  
 860 zone, their model ultimately lacks regularizations that remove mesh dependence.

861 As noted in Section 1.2 of the Introduction, a variety of continuum theories have  
 862 been developed to explain the general rate- and state-like behavior of deformation in faults

863 and shear zones (e.g. Sleep, 1997; Braeck & Podladchikov, 2007; John et al., 2009; Thiel-  
864 mann et al., 2015; Thielmann, 2018; Rozel et al., 2011; Barbot, 2019; Niemeijer & Spiers,  
865 2007; Chen & Spiers, 2016; Van den Ende et al., 2018; Roubíček, 2014; Lyakhovsky et  
866 al., 2011; Lyakhovsky & Ben-Zion, 2014b, 2014a; Lyakhovsky et al., 2016; Kurzon et al.,  
867 2019, 2020; Poulet et al., 2014; Veveakis et al., 2014; Alevizos et al., 2014; Rattez, Ste-  
868 fanou, & Sulem, 2018; Rattez, Stefanou, Sulem, Veveakis, & Poulet, 2018; Pozzi et al.,  
869 2021). We note again that an internal length scale in these models typically arises from  
870 the inclusion of a diffusion process (of e.g. temperature, pore pressure) but that may not  
871 always be adjusted to meet the constraints imposed by scale and computational power  
872 without changing the outcome of the model. In our proposed formulation an artificial  
873 diffusion process acts directly on the anelastic shear strain rate, resulting in a robust and  
874 controllable internal length scale.

875 In this last respect our work is preceded by nearly 25 years by Sleep (1997). In this  
876 work Sleep combined and extended earlier works (Sleep, 1995; Segall & Rice, 1995; Linker  
877 & Dieterich, 1992; Chester, 1994, 1995) in which rate and state friction was interpreted  
878 as the product of crack generation and healing, associated rheological weakening, and  
879 dissipative heating. This physical reasoning resulted in a model that contains only quan-  
880 tities that are either directly measurable or can be modeled by independent methods.  
881 This contrasts with our purely mathematical argumentation that serves to retain close  
882 correspondence to the original phenomenological description of rate and state dependent  
883 sliding on a frictional interface. Sleep (1997) neglects the fluxes and associated spatial  
884 gradients of the pore fluid but does include heat diffusion, which they note does how-  
885 ever not play a significant role at the scale of their numerical experiments. Instead, re-  
886 sembling our approach, they impose an artificial length scale and forced strain distribu-  
887 tion by explicit mollification of the anelastic shear strain rate with a Gaussian kernel.  
888 This leads to an aging law (Equation 53 in Sleep (1997)) that is structurally identical  
889 to our result (15). Like us, they find that strain localization can only occur when  $a <$   
890  $b$ , and that a rate-strengthening effect that activates at high strain rate leads to strain  
891 delocalization. With respect to Sleep’s valuable contribution, in this work we provide  
892 a more complete argumentation for this type of spatial regularization and analysis of the  
893 resulting patterns of strain localization and delocalization over the seismic cycle.

## 5.5 Assumptions and their impact on future work

We proposed our model in a very general three-dimensional continuum mechanics framework, but for simplicity have considered only a small fault neighborhood in which in-plane variations of fault properties can be neglected (Section 2.2) so that the model becomes effectively one-dimensional. This same assumption was also taken in the numerical models that we have used in our analysis. The assumption is clearly violated around fault branches, at fault kinks or on rough faults, and near the fault or rupture tip. We note however that rate and state friction was proposed based on laboratory studies that also neglect these geometrical complexities. Although rate and state faults with branches and kinks are still largely non-standard in present-day numerical modeling studies, plenty of attention has been given to the critical nucleation patch and the structure of the cohesive zone near the rupture tip (e.g. Rice, 1993; Cocco & Bizzarri, 2002; Cocco et al., 2004; Rubin & Ampuero, 2005; Day et al., 2005; Lapusta & Liu, 2009; Viesca, 2016b, 2016a; Putelat et al., 2017). Given our main assumption, these features can only be accurately reproduced with our continuum formulation in higher-dimensional numerical models if the regularization length scale  $\lambda$  is significantly smaller than the length scales associated with the critical nucleation patch and the cohesive zone. In turn the cell size must be sufficient to resolve  $\lambda$ , and so we expect to need a grid resolution that is significantly higher than that of existing methods to simulate rate and state frictional interfaces. We have also seen that the diffusion process is associated with a smaller time scale, and thus, stricter time step constraints than the interfacial model. We note that both spatial and temporal resolution requirements already place challenging constraints on simulations of seismic and aseismic slip sequences (Erickson et al., 2020).

It seems prudent to first make a more detailed assessment of the computational demands and the techniques that may be required to meet the resolution requirements (e.g. adaptive mesh refinement, local adaptive time stepping). In the process of constructing higher-dimensional models one may first concentrate on the friendliest regions of parameter space, for example those that promote stable sliding, or undamped runaway localization as in Viesca (2016b, 2016a).

The temporal patterns of localization and delocalization that occur in our model yield testable predictions that neatly tie in to a recent surge in interest in similar patterns observed in the lab and in nature (e.g. Ben-Zion & Zaliapin, 2020; McBeck et al.,

2018; McBeck, Aiken, et al., 2020; McBeck, Ben-Zion, & Renard, 2020; McBeck et al.,  
 2021). It could be the scope of future research to reinterpret anelastic strain rate in our  
 model as a measure of the activity of a statistical distribution of cracks of various prop-  
 erties and compare to aforementioned lab and field observations. In this context, the de-  
 localization that is in our models induced by a rate-limiting Kelvin viscosity is reminis-  
 cent of the growth of off-fault fracture networks during dynamic rupture (e.g. Temple-  
 ton & Rice, 2008; K. Okubo et al., 2019; Gabriel et al., 2021).

## 6 Conclusions

In this work we have carefully constructed a coordinate-invariant and mesh-independent  
 transient visco-elastic continuum rheology that behaves in a way that is consistent with  
 rate and state friction on an interface. We have shown that inclusion of a diffusion-like  
 spatial regularization ensures a limit to strain localization and thus guarantees mesh con-  
 vergence. In a simplified 1D fault transect, important metrics of the seismic cycle – such  
 as slip rate and friction – are independent of the diffusion length scale associated with  
 the regularization. However, throughout this work we have assumed the regularization  
 length scale to be small compared to the length scales associated with other features of  
 interest, such as fault curvature or along-strike variations of slip rate and stress. There-  
 fore, going forward, high-resolution 2D or 3D numerical models are required to apply this  
 model to the study of the seismogenic behavior of emerging and evolving fault zone net-  
 works. Our continuum rheology resembles a reaction-diffusion equation for anelastic strain  
 rate. Processes described by such equations are ubiquitous in nature, and it is tempt-  
 ing to compare temporal patterns of localization and delocalization produced by our model  
 with natural observations.

## Acknowledgments

This research has been supported by the European Union’s Horizon 2020 Research and  
 Innovation Programme under the ERC StG TEAR, grant no. 852992. CP acknowledges  
 additional financial support by Swiss National Science Foundation grant 200021-169880.  
 PS acknowledges financial support from the Swiss University Conference and the Swiss  
 Council of Federal Institutes of Technology through the Platform for Advanced Scien-  
 tific Computing (PASC) program. A.-A.G. acknowledges additional support by the Eu-  
 ropean Union’s Horizon 2020 Research and Innovation Programme under ChEESE, grant

no. 823844 and the German Research Foundation (DFG projects grants no. GA 2465/2-1, GA 2465/3-1). None of the authors declare any competing interests or financial conflicts. All scripts used to generate the figures and their underlying data are available in the supplementary materials. We depend on the MIT-licensed ‘Scientific Colour Maps’ package (Crameri, 2021) for distortion-free representation of the model results – also for readers with color vision deficiencies (Crameri et al., 2020).

## Appendix A Solution procedure

We discretize the Laplacian using a standard second-order accurate central difference stencil, with natural boundary conditions of the same accuracy implemented by staggering the fields with respect to the physical domain walls. The problem size is halved by exploiting symmetry across the shear zone. Integrals are evaluated using a midpoint rule. This gives the discrete system

$$\begin{aligned}\dot{\tilde{\zeta}} &= \mathbf{g}(\tilde{\zeta}, \tilde{f}) \\ \dot{\tilde{f}} &= \mathbf{h}(\tilde{\zeta}, \tilde{f}),\end{aligned}$$

where tildes indicate approximate space-discrete quantities and numerical arrays are indicated in bold face. We form a symbolic rules for computing the Jacobian matrix  $\mathbf{J}$  of this system of non-linear space-discrete equations,

$$\mathbf{J}(\tilde{\zeta}, \tilde{f}) = \begin{bmatrix} \nabla_{\tilde{\zeta}} \mathbf{g}(\tilde{\zeta}, \tilde{f}) & \nabla_{\tilde{f}} \mathbf{g}(\tilde{\zeta}, \tilde{f}) \\ \nabla_{\tilde{\zeta}} \mathbf{h}(\tilde{\zeta}, \tilde{f}) & \nabla_{\tilde{f}} \mathbf{h}(\tilde{\zeta}, \tilde{f}) \end{bmatrix},$$

with the upper left block a dense  $N \times N$  matrix with a dominant sparse band structure ( $N$  being the problem size), the lower right block a  $1 \times 1$  empty matrix, and the off-diagonal blocks densely populated vectors of compatible shape. The system is then linearized as

$$\mathbf{d} \begin{bmatrix} \dot{\tilde{\zeta}} \\ \dot{\tilde{f}} \end{bmatrix} = \mathbf{J}(\tilde{\zeta}, \tilde{f}) \mathbf{d} \begin{bmatrix} \tilde{\zeta} \\ \tilde{f} \end{bmatrix}$$

and the smallest time scale  $S_t(\tilde{\zeta}, \tilde{f})$  to be resolved is computed as the reciprocal of the largest eigenvalue of the Jacobian matrix  $\mathbf{J}$ . The actual time step  $\Delta_t$  is computed as some fixed fraction of  $S_t$ , optionally bounded by a maximum value and/or maximum growth rate to prevent time step overestimation as the time scale increases. The equations are discretized in time with forward and backward Euler schemes, both first-order accurate,

987 respectively as

$$988 \begin{bmatrix} \tilde{\zeta}^{k+1} \\ \tilde{f}^{k+1} \end{bmatrix} = \begin{bmatrix} \tilde{\zeta}^k \\ \tilde{f}^k \end{bmatrix} + \Delta_t \begin{bmatrix} \mathbf{g}(\tilde{\zeta}^k, \tilde{f}^k) \\ \mathbf{h}(\tilde{\zeta}^k, \tilde{f}^k) \end{bmatrix} \quad (\text{A1})$$

$$989 \mathbf{f} = \begin{bmatrix} \tilde{\zeta}^{k+1} \\ \tilde{f}^{k+1} \end{bmatrix} - \begin{bmatrix} \tilde{\zeta}^k \\ \tilde{f}^k \end{bmatrix} - \Delta_t \begin{bmatrix} \mathbf{g}(\tilde{\zeta}^{k+1}, \tilde{f}^{k+1}) \\ \mathbf{h}(\tilde{\zeta}^{k+1}, \tilde{f}^{k+1}) \end{bmatrix} = \mathbf{0}. \quad (\text{A2})$$

990 Our algorithm makes an explicit-in-time prediction using (A1) and evaluates the  $l_2$  norm  
 991 of the implicit-in-time residual  $\mathbf{f}$ . It includes the possibility to perform Newton-Raphson  
 992 iterations using the Jacobian  $\mathbf{J}$  to keep the residual bounded, although we find it to be  
 993 more efficient to experimentally set the dimensionless time step  $\Delta_t/S_t$  sufficiently small  
 994 (e.g. 0.1) to never cause tolerances to be violated. This value is then taken to correspond  
 995 to a stable time step size of the explicit problem.  
 996

997 We make our algorithms and scripts to produce figures available as Wolfram Math-  
 998 ematica (Wolfram Research, Inc., 2017) notebooks in the Supplementary Materials.

## 999 References

- 1000 Abdallah, Y., Sulem, J., & Stefanou, I. (2020). Compaction banding in high-porosity  
 1001 carbonate rocks: 2. a gradient-dependent plasticity model. *Journal of Geophys-*  
 1002 *ical Research: Solid Earth*, 125(12), e2020JB020610.
- 1003 Alevizos, S., Poulet, T., & Veveakis, E. (2014). Thermo-poro-mechanics of chemi-  
 1004 cally active creeping faults. 1: Theory and steady state considerations. *Journal*  
 1005 *of Geophysical Research: Solid Earth*, 119(6), 4558–4582.
- 1006 Andrews, D. (1999). Test of two methods for faulting in finite-difference calculations.  
 1007 *Bulletin of the Seismological Society of America*, 89(4), 931–937.
- 1008 Bak, P., & Tang, C. (1989). Earthquakes as a self-organized critical phenomenon.  
 1009 *Journal of Geophysical Research: Solid Earth*, 94(B11), 15635–15637. doi:  
 1010 <https://doi.org/10.1029/JB094iB11p15635>
- 1011 Barbot, S. (2019). Modulation of fault strength during the seismic cycle by grain-  
 1012 size evolution around contact junctions. *Tectonophysics*, 765, 129 - 145. doi:  
 1013 <https://doi.org/10.1016/j.tecto.2019.05.004>
- 1014 Barry, D., Barry, S., & Culligan-Hensley, P. (1995). Algorithm 743: Wapr—a for-  
 1015 tran routine for calculating real values of the w-function. *ACM Transactions*  
 1016 *on Mathematical Software (TOMS)*, 21(2), 172–181.

- 1017 Barry, D., Culligan-Hensley, P., & Barry, S. (1995). Real values of the w-function.  
1018 *ACM Transactions on Mathematical Software (TOMS)*, *21*(2), 161–171.
- 1019 Barth, N. C., Boulton, C., Carpenter, B. M., Batt, G. E., & Toy, V. G. (2013). Slip  
1020 localization on the southern alpine fault, new zealand. *Tectonics*, *32*(3), 620–  
1021 640. doi: <https://doi.org/10.1002/tect.20041>
- 1022 Bažant, Z. P., Belytschko, T. B., & Chang, T.-P. (1984). Continuum theory for  
1023 strain-softening. *Journal of Engineering Mechanics*, *110*(12), 1666–1692.
- 1024 Bažant, Z. P., & Jirásek, M. (2002). Nonlocal integral formulations of plasticity and  
1025 damage: survey of progress. *Journal of engineering mechanics*, *128*(11), 1119–  
1026 1149.
- 1027 Ben-Zion, Y., & Rice, J. R. (1997). Dynamic simulations of slip on a smooth fault in  
1028 an elastic solid. *Journal of Geophysical Research: Solid Earth*, *102*(B8), 17771–  
1029 17784. doi: [10.1029/97JB01341](https://doi.org/10.1029/97JB01341)
- 1030 Ben-Zion, Y., & Zaliapin, I. (2020). Localization and coalescence of seismicity before  
1031 large earthquakes. *Geophysical Journal International*, *223*(1), 561–583. doi: [10](https://doi.org/10.1093/gji/ggaa315)  
1032 [.1093/gji/ggaa315](https://doi.org/10.1093/gji/ggaa315)
- 1033 Bowden, F. P., & Tabor, D. (1966, dec). Friction, lubrication and wear: a survey of  
1034 work during the last decade. *British Journal of Applied Physics*, *17*(12), 1521–  
1035 1544. doi: [10.1088/0508-3443/17/12/301](https://doi.org/10.1088/0508-3443/17/12/301)
- 1036 Brace, W., & Byerlee, J. (1966). Stick-slip as a mechanism for earthquakes. *Science*,  
1037 *153*(3739), 990–992.
- 1038 Braeck, S., & Podladchikov, Y. Y. (2007, Mar). Spontaneous thermal runaway as an  
1039 ultimate failure mechanism of materials. *Phys. Rev. Lett.*, *98*, 095504. doi: [10](https://doi.org/10.1103/PhysRevLett.98.095504)  
1040 [.1103/PhysRevLett.98.095504](https://doi.org/10.1103/PhysRevLett.98.095504)
- 1041 Broadbridge, P., & Bradshaw-Hajek, B. H. (2016, Jul 16). Exact solutions for lo-  
1042 gistic reaction–diffusion equations in biology. *Zeitschrift für angewandte Math-*  
1043 *ematik und Physik*, *67*(4), 93. doi: [10.1007/s00033-016-0686-3](https://doi.org/10.1007/s00033-016-0686-3)
- 1044 Burghardt, J., Brannon, R., & Guilkey, J. (2012). A nonlocal plasticity formu-  
1045 lation for the material point method. *Computer methods in applied mechanics*  
1046 *and engineering*, *225*, 55–64.
- 1047 Chen, J., & Spiers, C. J. (2016). Rate and state frictional and healing behavior  
1048 of carbonate fault gouge explained using microphysical model. *Journal of Geo-*  
1049 *physical Research: Solid Earth*, *121*(12), 8642–8665.

- 1050 Chester, F. M. (1994). Effects of temperature on friction: Constitutive equations  
 1051 and experiments with quartz gouge. *Journal of Geophysical Research: Solid*  
 1052 *Earth*, *99*(B4), 7247–7261.
- 1053 Chester, F. M. (1995). A rheologic model for wet crust applied to strike-slip faults.  
 1054 *Journal of Geophysical Research: Solid Earth*, *100*(B7), 13033–13044.
- 1055 Cocco, M., & Bizzarri, A. (2002). On the slip-weakening behavior of rate- and state  
 1056 dependent constitutive laws. *Geophysical Research Letters*, *29*(11), 11-1-11-4.  
 1057 doi: 10.1029/2001GL013999
- 1058 Cocco, M., Bizzarri, A., & Tinti, E. (2004). Physical interpretation of the breakdown  
 1059 process using a rate- and state-dependent friction law. *Tectonophysics*, *378*(3),  
 1060 241 - 262. (Physics of Active Faults - Theory, Observation and Experiments)  
 1061 doi: <https://doi.org/10.1016/j.tecto.2003.09.015>
- 1062 Cramer, F. (2021, September). *Scientific colour maps*. Zenodo. Retrieved from  
 1063 <https://doi.org/10.5281/zenodo.5501399> doi: 10.5281/zenodo.5501399
- 1064 Cramer, F., Shephard, G. E., & Heron, P. J. (2020). The misuse of colour in science  
 1065 communication. *Nature communications*, *11*(1), 1–10.
- 1066 Day, S. M., Dalguer, L. A., Lapusta, N., & Liu, Y. (2005). Comparison of fi-  
 1067 nite difference and boundary integral solutions to three-dimensional sponta-  
 1068 neous rupture. *Journal of Geophysical Research: Solid Earth*, *110*(B12). doi:  
 1069 10.1029/2005JB003813
- 1070 de Borst, R., & Duretz, T. (2020). On viscoplastic regularisation of strain-softening  
 1071 rocks and soils. *International Journal for Numerical and Analytical Methods in*  
 1072 *Geomechanics*, *44*(6), 890-903. doi: <https://doi.org/10.1002/nag.3046>
- 1073 de Borst, R., & Mühlhaus, H.-B. (1992). Gradient-dependent plasticity: Formulation  
 1074 and algorithmic aspects. *International Journal for Numerical Methods in Engi-*  
 1075 *neering*, *35*(3), 521-539. doi: 10.1002/nme.1620350307
- 1076 Dieterich, J. H. (1978, Jul 01). Time-dependent friction and the mechanics of stick-  
 1077 slip. *pure and applied geophysics*, *116*(4), 790–806. doi: 10.1007/BF00876539
- 1078 Dieterich, J. H. (1979a). Modeling of rock friction: 1. experimental results and  
 1079 constitutive equations. *Journal of Geophysical Research: Solid Earth*, *84*(B5),  
 1080 2161–2168. doi: 10.1029/JB084iB05p02161
- 1081 Dieterich, J. H. (1979b). Modeling of rock friction: 2. simulation of preseismic  
 1082 slip. *Journal of Geophysical Research: Solid Earth*, *84*(B5), 2169–2175. doi:

- 1083 10.1029/JB084iB05p02169
- 1084 Dieterich, J. H., & Kilgore, B. D. (1994, Mar 01). Direct observation of frictional  
 1085 contacts: New insights for state-dependent properties. *pure and applied geo-*  
 1086 *physics*, *143*(1), 283–302. doi: 10.1007/BF00874332
- 1087 Drucker, D. C., & Prager, W. (1952). Soil mechanics and plastic analysis or limit de-  
 1088 sign. *Quarterly of applied mathematics*, *10*(2), 157–165.
- 1089 Duretz, T., de Borst, R., & Le Pourhiet, L. (2019). Finite thickness of shear bands  
 1090 in frictional viscoplasticity and implications for lithosphere dynamics. *Geo-*  
 1091 *chemistry, Geophysics, Geosystems*. doi: 10.1029/2019GC008531
- 1092 Duretz, T., de Borst, R., & Yamato, P. (2021). Modeling lithospheric deforma-  
 1093 tion using a compressible visco-elasto-viscoplastic rheology and the effective  
 1094 viscosity approach. *Geochemistry, Geophysics, Geosystems*, *22*(8). doi:  
 1095 <https://doi.org/10.1029/2021GC009675>
- 1096 Duretz, T., de Borst, R., Yamato, P., & Le Pourhiet, L. (2020). Toward robust  
 1097 and predictive geodynamic modeling: The way forward in frictional plastic-  
 1098 ity. *Geophysical Research Letters*, *47*(5), e2019GL086027. (e2019GL086027  
 1099 10.1029/2019GL086027) doi: 10.1029/2019GL086027
- 1100 Duretz, T., Souche, A., de Borst, R., & Le Pourhiet, L. (2018). The benefits of using  
 1101 a consistent tangent operator for viscoelastoplastic computations in geodynam-  
 1102 ics. *Geochemistry, Geophysics, Geosystems*, *19*(12), 4904–4924.
- 1103 Engelen, R. A., Geers, M. G., & Baaijens, F. P. (2003). Nonlocal implicit gradient-  
 1104 enhanced elasto-plasticity for the modelling of softening behaviour. *Interna-*  
 1105 *tional Journal of Plasticity*, *19*(4), 403 - 433. doi: [https://doi.org/10.1016/](https://doi.org/10.1016/S0749-6419(01)00042-0)  
 1106 [S0749-6419\(01\)00042-0](https://doi.org/10.1016/S0749-6419(01)00042-0)
- 1107 Erickson, B. A., Jiang, J., Barall, M., Lapusta, N., Dunham, E. M., Harris, R., . . .  
 1108 Wei, M. (2020, 01). The Community Code Verification Exercise for Simulating  
 1109 Sequences of Earthquakes and Aseismic Slip (SEAS). *Seismological Research*  
 1110 *Letters*. doi: 10.1785/0220190248
- 1111 Faulkner, D., Mitchell, T., Jensen, E., & Cembrano, J. (2011). Scaling of fault dam-  
 1112 age zones with displacement and the implications for fault growth processes.  
 1113 *Journal of Geophysical Research: Solid Earth*, *116*(B5).
- 1114 Fisher, R. A. (1937). The wave of advance of advantageous genes. *Annals of Eugen-*  
 1115 *ics*, *7*(4), 355-369. doi: 10.1111/j.1469-1809.1937.tb02153.x

- 1116 Fritsch, F. N., Shafer, R., & Crowley, W. (1973). Algorithm 443: Solution of the  
 1117 transcendental equation  $we^w = x$ . *Communications of the ACM*, *16*(2), 123–  
 1118 124.
- 1119 Gabriel, A.-A., Ampuero, J.-P., Dalguer, L. A., & Mai, P. M. (2012). The transition  
 1120 of dynamic rupture styles in elastic media under velocity-weakening friction.  
 1121 *Journal of Geophysical Research: Solid Earth*, *117*(B9).
- 1122 Gabriel, A.-A., Li, D., Chiocchetti, S., Tavelli, M., Peshkov, I., Romenski, E., &  
 1123 Dumbser, M. (2021). A unified first-order hyperbolic model for nonlinear  
 1124 dynamic rupture processes in diffuse fracture zones. *Philosophical Transactions*  
 1125 *of the Royal Society A*, *379*(2196), 20200130.
- 1126 Gilding, B., & Kersner, R. (2005, 03). A fisher/kpp-type equation with density-  
 1127 dependent diffusion and convection: travelling-wave solutions. *Journal of*  
 1128 *Physics A: Mathematical and General*, *38*, 3367. doi: 10.1088/0305-4470/38/  
 1129 15/009
- 1130 Godunov, S., & Romenskii, E. (1972). Nonstationary equations of nonlinear elastic-  
 1131 ity theory in eulerian coordinates. *Journal of Applied Mechanics and Technical*  
 1132 *Physics*, *13*(6), 868–884.
- 1133 Godunov, S. K., & Romenskii, E. (2003). *Elements of continuum mechanics and*  
 1134 *conservation laws*. Springer Science & Business Media.
- 1135 Granier, T. (1985). Origin, damping, and pattern of development of faults in gran-  
 1136 ite. *Tectonics*, *4*(7), 721–737. doi: <https://doi.org/10.1029/TC004i007p00721>
- 1137 Herrendörfer, R., Gerya, T., & Van Dinther, Y. (2018). An invariant rate-and  
 1138 state-dependent friction formulation for viscoelastoplastic earthquake cycle  
 1139 simulations. *Journal of Geophysical Research: Solid Earth*, *123*(6), 5018–5051.
- 1140 Hobbs, B. E., Mühlhaus, H.-B., & Ord, A. (1990). Instability, softening and local-  
 1141 ization of deformation. *Geological Society, London, Special Publications*, *54*(1),  
 1142 143–165. doi: 10.1144/GSL.SP.1990.054.01.15
- 1143 Ida, Y. (1972). Cohesive force across the tip of a longitudinal-shear crack and grif-  
 1144 fith’s specific surface energy. *Journal of Geophysical Research*, *77*(20), 3796–  
 1145 3805.
- 1146 Jiang, J., & Lapusta, N. (2016). Deeper penetration of large earthquakes on seismi-  
 1147 cally quiescent faults. *Science*, *352*(6291), 1293–1297.
- 1148 Jirásek, M. (1998). Nonlocal models for damage and fracture: comparison of

- 1149 approaches. *International Journal of Solids and Structures*, *35*(31-32), 4133–  
1150 4145.
- 1151 Jirásek, M., & Rolshoven, S. (2009a). Localization properties of strain-softening gra-  
1152 dient plasticity models. part ii: Theories with gradients of internal variables.  
1153 *International Journal of Solids and Structures*, *46*(11-12), 2239–2254.
- 1154 Jirásek, M., & Rolshoven, S. (2009b). Localization properties of strain-softening gra-  
1155 dient plasticity models. part i: Strain-gradient theories. *International Journal*  
1156 *of Solids and Structures*, *46*(11-12), 2225–2238.
- 1157 Johansson, F. (2020). Computing the lambert w function in arbitrary-precision com-  
1158 plex interval arithmetic. *Numerical Algorithms*, *83*(1), 221–242.
- 1159 John, T., Medvedev, S., Rüpke, L. H., Andersen, T. B., Podladchikov, Y. Y., &  
1160 Austrheim, H. (2009). Generation of intermediate-depth earthquakes by self-  
1161 localizing thermal runaway. *Nature Geoscience*, *2*, 137–140.
- 1162 Katz, Y., Weinberger, R., & Aydin, A. (2004). Geometry and kinematic evolution of  
1163 riedel shear structures, capitol reef national park, utah. *Journal of Structural*  
1164 *Geology*, *26*(3), 491-501. doi: <https://doi.org/10.1016/j.jsg.2003.08.003>
- 1165 Kaus, B. J. (2010). Factors that control the angle of shear bands in geodynamic nu-  
1166 merical models of brittle deformation. *Tectonophysics*, *484*(1), 36 - 47. (Quan-  
1167 titative modelling of geological processes) doi: [https://doi.org/10.1016/j.tecto](https://doi.org/10.1016/j.tecto.2009.08.042)  
1168 [.2009.08.042](https://doi.org/10.1016/j.tecto.2009.08.042)
- 1169 Kiefer, B., Waffenschmidt, T., Sprave, L., & Menzel, A. (2018). A gradient-enhanced  
1170 damage model coupled to plasticity—multi-surface formulation and algorithmic  
1171 concepts. *International Journal of Damage Mechanics*, *27*(2), 253-295. doi:  
1172 [10.1177/1056789516676306](https://doi.org/10.1177/1056789516676306)
- 1173 Kolmogorov, A. N., Petrovskii, I. G., & Piskunov, N. S. (1937). A study of the  
1174 diffusion equation with increase in the amount of substance, and its applica-  
1175 tion to a biological problem. In V. Tikhomirov (Ed.), *Selected works of a.n.*  
1176 *kolmogorov 1 (1991)* (pp. 242–270). Kluwer.
- 1177 Kuhn, C., Schlüter, A., & Müller, R. (2015). On degradation functions in phase field  
1178 fracture models. *Computational Materials Science*, *108*, 374–384.
- 1179 Kurzon, I., Lyakhovskiy, V., & Ben-Zion, Y. (2019). Dynamic rupture and seismic  
1180 radiation in a damage–breakage rheology model. *Pure and Applied Geophysics*,  
1181 *176*(3), 1003–1020.

- 1182 Kurzon, I., Lyakhovsky, V., & Ben-Zion, Y. (2020, 10). Earthquake source proper-  
 1183 ties from analysis of dynamic ruptures and far-field seismic waves in a damage-  
 1184 breakage model. *Geophysical Journal International*, *224*(3), 1793-1810. doi:  
 1185 10.1093/gji/ggaa509
- 1186 Lapusta, N., & Liu, Y. (2009). Three-dimensional boundary integral modeling of  
 1187 spontaneous earthquake sequences and aseismic slip. *Journal of Geophysical*  
 1188 *Research: Solid Earth*, *114*(B9). doi: 10.1029/2008JB005934
- 1189 Lapusta, N., Rice, J. R., Ben-Zion, Y., & Zheng, G. (2000). Elastodynamic analysis  
 1190 for slow tectonic loading with spontaneous rupture episodes on faults with  
 1191 rate- and state-dependent friction. *Journal of Geophysical Research: Solid*  
 1192 *Earth*, *105*(B10), 23765-23789. doi: 10.1029/2000JB900250
- 1193 Le Pourhiet, L. (2013). Strain localization due to structural softening during pres-  
 1194 sure sensitive rate independent yielding. *Bulletin de la Société géologique de*  
 1195 *France*, *184*(4-5), 357-371.
- 1196 Li, D., & Liu, Y. (2017). Modeling slow-slip segmentation in cascadia subduction  
 1197 zone constrained by tremor locations and gravity anomalies. *Journal of Geo-*  
 1198 *physical Research: Solid Earth*, *122*(4), 3138-3157.
- 1199 Li, Y., & Wu, Y. (2008, 07). Stability of travelling waves with noncritical speeds  
 1200 for double degenerate fisher-type equations. *Discrete and Continuous Dynamical*  
 1201 *Systems - Series B*, *10*, 149-170. doi: 10.3934/dcdsb.2008.10.149
- 1202 Linker, M., & Dieterich, J. H. (1992). Effects of variable normal stress on rock  
 1203 friction: Observations and constitutive equations. *Journal of Geophysical Re-*  
 1204 *search: Solid Earth*, *97*(B4), 4923-4940.
- 1205 Locatelli, M., Verlaguet, A., Agard, P., Federico, L., & Angiboust, S. (2018).  
 1206 Intermediate-depth brecciation along the subduction plate interface (monviso  
 1207 eclogite, w. alps). *Lithos*, *320*, 378-402.
- 1208 Locatelli, M., Verlaguet, A., Agard, P., Pettke, T., & Federico, L. (2019). Fluid  
 1209 pulses during stepwise brecciation at intermediate subduction depths (monviso  
 1210 eclogites, w. alps): First internally then externally sourced. *Geochemistry,*  
 1211 *geophysics, geosystems*, *20*(11), 5285-5318.
- 1212 Lyakhovsky, V., & Ben-Zion, Y. (2014a). A continuum damage-breakage faulting  
 1213 model and solid-granular transitions. *Pure and Applied Geophysics*, *171*(11),  
 1214 3099-3123.

- 1215 Lyakhovsky, V., & Ben-Zion, Y. (2014b). Damage–breakage rheology model and  
 1216 solid-granular transition near brittle instability. *Journal of the Mechanics and*  
 1217 *Physics of Solids*, *64*, 184–197.
- 1218 Lyakhovsky, V., Ben-Zion, Y., Ilchev, A., & Mendecki, A. (2016). Dynamic rup-  
 1219 ture in a damage-breakage rheology model. *Geophysical Journal International*,  
 1220 *206*(2), 1126–1143.
- 1221 Lyakhovsky, V., Hamiel, Y., & Ben-Zion, Y. (2011). A non-local visco-elastic dam-  
 1222 age model and dynamic fracturing. *Journal of the Mechanics and Physics of*  
 1223 *Solids*, *59*(9), 1752–1776.
- 1224 Mair, K., & Marone, C. (1999). Friction of simulated fault gouge for a wide range of  
 1225 velocities and normal stresses. *Journal of Geophysical Research: Solid Earth*,  
 1226 *104*(B12), 28899–28914. doi: 10.1029/1999JB900279
- 1227 Malaguti, L., & Ruggerini, S. (2010, 08). Asymptotic speed of propagation for fisher-  
 1228 type degenerate reaction-diffusion-convection equations. *Advanced Nonlinear*  
 1229 *Studies*, *10*. doi: 10.1515/ans-2010-0306
- 1230 Marone, C. (1998). The effect of loading rate on static friction and the rate of fault  
 1231 healing during the earthquake cycle. *Nature*, *391*(6662), 69–72. doi: 10.1038/  
 1232 34157
- 1233 McBeck, J. A., Aiken, J. M., Mathiesen, J., Ben-Zion, Y., & Renard, F. (2020). De-  
 1234 formation precursors to catastrophic failure in rocks. *Geophysical Research Let-*  
 1235 *ters*, *47*(24), e2020GL090255.
- 1236 McBeck, J. A., Ben-Zion, Y., & Renard, F. (2020). The mixology of precursory  
 1237 strain partitioning approaching brittle failure in rocks. *Geophysical Journal In-*  
 1238 *ternational*, *221*(3), 1856–1872.
- 1239 McBeck, J. A., Kobchenko, M., Hall, S. A., Tudisco, E., Cordonnier, B., Meakin,  
 1240 P., & Renard, F. (2018). Investigating the onset of strain localization within  
 1241 anisotropic shale using digital volume correlation of time-resolved x-ray micro-  
 1242 tomography images. *Journal of Geophysical Research: Solid Earth*, *123*(9),  
 1243 7509–7528.
- 1244 McBeck, J. A., Zhu, W., & Renard, F. (2021). The competition between fracture  
 1245 nucleation, propagation, and coalescence in dry and water-saturated crystalline  
 1246 rock. *Solid Earth*, *12*(2), 375–387.
- 1247 Mühlhaus, H.-B., & Aifantis, E. (1991). A variational principle for gradient plastic-

- 1248 ity. *International Journal of Solids and Structures*, 28(7), 845–857.
- 1249 Needleman, A. (1988). Material rate dependence and mesh sensitivity in localization  
1250 problems. *Computer Methods in Applied Mechanics and Engineering*, 67(1), 69  
1251 - 85. doi: [https://doi.org/10.1016/0045-7825\(88\)90069-2](https://doi.org/10.1016/0045-7825(88)90069-2)
- 1252 Niemeijer, A., & Spiers, C. (2007). A microphysical model for strong velocity weak-  
1253 ening in phyllosilicate-bearing fault gouges. *Journal of Geophysical Research:*  
1254 *Solid Earth*, 112(B10).
- 1255 Okubo, K., Bhat, H. S., Rougier, E., Marty, S., Schubnel, A., Lei, Z., . . . Klinger, Y.  
1256 (2019). Dynamics, radiation, and overall energy budget of earthquake rupture  
1257 with coseismic off-fault damage. *Journal of Geophysical Research: Solid Earth*,  
1258 124(11), 11771-11801. doi: 10.1029/2019JB017304
- 1259 Okubo, P. G. (1989). Dynamic rupture modeling with laboratory-derived consti-  
1260 tutive relations. *Journal of Geophysical Research: Solid Earth*, 94(B9), 12321–  
1261 12335.
- 1262 Passelègue, F. X., Almakari, M., Dublanchet, P., Barras, F., Fortin, J., & Violay,  
1263 M. (2020). Initial effective stress controls the nature of earthquakes. *Nature*  
1264 *communications*, 11(1), 1–8.
- 1265 Passelègue, F. X., Spagnuolo, E., Violay, M., Nielsen, S., Di Toro, G., & Schubnel,  
1266 A. (2016). Frictional evolution, acoustic emissions activity, and off-fault dam-  
1267 age in simulated faults sheared at seismic slip rates. *Journal of Geophysical*  
1268 *Research: Solid Earth*, 121(10), 7490–7513.
- 1269 Peerlings, R. H. J., de Borst, R., Brekelmans, W. A. M., & De Vree, J. H. P. (1996).  
1270 Gradient enhanced damage for quasi-brittle materials. *International Journal*  
1271 *for Numerical Methods in Engineering*, 39(19), 3391-3403. doi: 10.1002/(SICI)  
1272 1097-0207(19961015)39:19<3391::AID-NME7>3.0.CO;2-D
- 1273 Peirce, D., Asaro, R. J., & Needleman, A. (1983). Material rate dependence and  
1274 localized deformation in crystalline solids. *Acta metallurgica*, 31(12), 1951–  
1275 1976.
- 1276 Perez-Silva, A., Li, D., Gabriel, A.-A., & Kaneko, Y. (2021). 3d modeling of long-  
1277 term slow slip events along the flat-slab segment in the guerrero seismic gap,  
1278 mexico. *Geophysical Research Letters*, 48(13), e2021GL092968.
- 1279 Perrin, C., Manighetti, I., & Gaudemer, Y. (2016). Off-fault tip splay networks:  
1280 A genetic and generic property of faults indicative of their long-term propa-

- 1281 gation. *Comptes Rendus Geoscience*, 348(1), 52-60. (From past to current  
1282 tectonics) doi: <https://doi.org/10.1016/j.crte.2015.05.002>
- 1283 Petrovskii, S., & Li, B.-L. (2003). An exactly solvable model of population dynam-  
1284 ics with density-dependent migrations and the allee effect. *Mathematical Bio-*  
1285 *sciences*, 186(1), 79 - 91. doi: [https://doi.org/10.1016/S0025-5564\(03\)00098](https://doi.org/10.1016/S0025-5564(03)00098)  
1286 -1
- 1287 Petrovskii, S. V., & Li, B.-L. (2006). *Exactly solvable models of biological invasion*.  
1288 Chapman and Hall/CRC.
- 1289 Pijaudier-Cabot, G., & Bazant, Z. P. (1987). Nonlocal damage theory. *Journal of*  
1290 *engineering mechanics*, 113(10), 1512–1533.
- 1291 Poulet, T., Veveakis, E., Regenauer-Lieb, K., & Yuen, D. A. (2014). Thermo-poro-  
1292 mechanics of chemically active creeping faults: 3. the role of serpentinite in  
1293 episodic tremor and slip sequences, and transition to chaos. *Journal of Geo-*  
1294 *physical Research: Solid Earth*, 119(6), 4606–4625.
- 1295 Pozzi, G., De Paola, N., Nielsen, S. B., Holdsworth, R. E., & Bowen, L. (2018, 05).  
1296 A new interpretation for the nature and significance of mirror-like surfaces in  
1297 experimental carbonate-hosted seismic faults. *Geology*, 46(7), 583-586. doi:  
1298 10.1130/G40197.1
- 1299 Pozzi, G., De Paola, N., Nielsen, S. B., Holdsworth, R. E., Tesei, T., Thieme, M.,  
1300 & Demouchy, S. (2021). Coseismic fault lubrication by viscous deformation.  
1301 *Nature Geoscience*, 14(6), 437–442.
- 1302 Pozzi, G., Paola, N. D., Holdsworth, R. E., Bowen, L., Nielsen, S. B., & Dempsey,  
1303 E. D. (2019). Coseismic ultramylonites: An investigation of nanoscale viscous  
1304 flow and fault weakening during seismic slip. *Earth and Planetary Science*  
1305 *Letters*, 516, 164 - 175. doi: <https://doi.org/10.1016/j.epsl.2019.03.042>
- 1306 Preuss, S., Ampuero, J. P., Gerya, T., & van Dinther, Y. (2020). Characteristics of  
1307 earthquake ruptures and dynamic off-fault deformation on propagating faults.  
1308 *Solid Earth*, 11(4), 1333–1360.
- 1309 Preuss, S., Herrendörfer, R., Gerya, T., Ampuero, J.-P., & van Dinther, Y.  
1310 (2019). Seismic and aseismic fault growth lead to different fault orienta-  
1311 tions. *Journal of Geophysical Research: Solid Earth*, 124(8), 8867-8889. doi:  
1312 10.1029/2019JB017324
- 1313 Putelat, T., Dawes, J., & Champneys, A. (2017). A phase-plane analysis of local-

- 1314            ized frictional waves. *Proceedings of the Royal Society A: Mathematical, Physi-*  
1315            *cal and Engineering Sciences*, 473(2203), 20160606.
- 1316 Rabinowicz, E. (1958). The intrinsic variables affecting the stick-slip process. *Pro-*  
1317            *ceedings of the Physical Society (1958-1967)*, 71(4), 668.
- 1318 Rattez, H., Stefanou, I., & Sulem, J. (2018). The importance of thermo-hydro-  
1319            mechanical couplings and microstructure to strain localization in 3d continua  
1320            with application to seismic faults. part i: Theory and linear stability analysis.  
1321            *Journal of the Mechanics and Physics of Solids*, 115, 54 - 76.
- 1322 Rattez, H., Stefanou, I., Sulem, J., Veveakis, M., & Poulet, T. (2018). The im-  
1323            portance of thermo-hydro-mechanical couplings and microstructure to strain  
1324            localization in 3d continua with application to seismic faults. part ii: Numer-  
1325            ical implementation and post-bifurcation analysis. *Journal of the Mechanics*  
1326            *and Physics of Solids*, 115, 1–29.
- 1327 Resnyansky, A., Romensky, E., & Bourne, N. (2003). Constitutive modeling of frac-  
1328            ture waves. *Journal of applied physics*, 93(3), 1537–1545.
- 1329 Rice, J. R. (1993). Spatio-temporal complexity of slip on a fault. *Journal of Geo-*  
1330            *physical Research: Solid Earth*, 98(B6), 9885-9907. doi: 10.1029/93JB00191
- 1331 Rice, J. R., & Ben-Zion, Y. (1996). Slip complexity in earthquake fault models. *Pro-*  
1332            *ceedings of the National Academy of Sciences*, 93(9), 3811–3818. doi: 10.1073/  
1333            pnas.93.9.3811
- 1334 Ritter, M. C., Rosenau, M., & Oncken, O. (2018). Growing faults in the lab: In-  
1335            sights into the scale dependence of the fault zone evolution process. *Tectonics*,  
1336            37(1), 140-153. doi: <https://doi.org/10.1002/2017TC004787>
- 1337 Ritter, M. C., Santimano, T., Rosenau, M., Leever, K., & Oncken, O. (2018).  
1338            Sandbox rheometry: Co-evolution of stress and strain in riedel- and critical  
1339            wedge-experiments. *Tectonophysics*, 722, 400-409. doi: [https://doi.org/](https://doi.org/10.1016/j.tecto.2017.11.018)  
1340            10.1016/j.tecto.2017.11.018
- 1341 Romenski, E., Reshetova, G., Peshkov, I., & Dumbser, M. (2020). Modeling wave-  
1342            fields in saturated elastic porous media based on thermodynamically compat-  
1343            ible system theory for two-phase solid-fluid mixtures. *Computers & Fluids*,  
1344            206, 104587. doi: <https://doi.org/10.1016/j.compfluid.2020.104587>
- 1345 Romenskii, E. (2007). Deformation model for brittle materials and the structure of  
1346            failure waves. *Journal of applied mechanics and technical physics*, 48(3), 437–

- 1347 444.
- 1348 Ross, Z. E., Idini, B., Jia, Z., Stephenson, O. L., Zhong, M., Wang, X., . . . others  
 1349 (2019). Hierarchical interlocked orthogonal faulting in the 2019 ridgecrest  
 1350 earthquake sequence. *Science*, *366*(6463), 346–351.
- 1351 Roubíček, T. (2014, 08). A note about the rate-and-state-dependent friction model  
 1352 in a thermodynamic framework of the Biot-type equation. *Geophysical Jour-*  
 1353 *nal International*, *199*(1), 286–295. doi: 10.1093/gji/ggu248
- 1354 Rozel, A., Ricard, Y., & Bercovici, D. (2011). A thermodynamically self-consistent  
 1355 damage equation for grain size evolution during dynamic recrystallization.  
 1356 *Geophysical Journal International*, *184*(2), 719–728.
- 1357 Rubin, A. M., & Ampuero, J.-P. (2005). Earthquake nucleation on (aging) rate and  
 1358 state faults. *Journal of Geophysical Research: Solid Earth*, *110*(B11).
- 1359 Ruina, A. L. (1980). *Friction laws and instabilities: A quasistatic analysis of some*  
 1360 *dry friction behaviour* (Unpublished doctoral dissertation). Ph.D. Thesis, Divi-  
 1361 sion of Engineering, Brown University, Providence RI.
- 1362 Ruina, A. L. (1983). Slip instability and state variable friction laws. *Jour-*  
 1363 *nal of Geophysical Research: Solid Earth*, *88*(B12), 10359–10370. doi:  
 1364 10.1029/JB088iB12p10359
- 1365 Sánchez-Garduño, F., & Maini, P. (1994). An approximation to a sharp type so-  
 1366 lution of a density-dependent reaction-diffusion equation. *Applied Mathematics*  
 1367 *Letters*, *7*(1), 47 - 51. doi: [https://doi.org/10.1016/0893-9659\(94\)90051-5](https://doi.org/10.1016/0893-9659(94)90051-5)
- 1368 Sánchez-Garduño, F., & Maini, P. (1995). Traveling wave phenomena in some degen-  
 1369 erate reaction-diffusion equations. *Journal of Differential Equations*, *117*(2),  
 1370 281 - 319. doi: <https://doi.org/10.1006/jdeq.1995.1055>
- 1371 Sánchez-Garduño, F., & Maini, P. (1997, Jun 01). Travelling wave phenomena in  
 1372 non-linear diffusion degenerate nagumo equations. *Journal of Mathematical Bi-*  
 1373 *ology*, *35*(6), 713–728. doi: 10.1007/s002850050073
- 1374 Sathiakumar, S., Barbot, S., & Hubbard, J. (2020). Earthquake cycles in fault-bend  
 1375 folds. *Journal of Geophysical Research: Solid Earth*, *125*(8), e2019JB018557.
- 1376 Savage, H. M., & Brodsky, E. E. (2011). Collateral damage: Evolution with dis-  
 1377 placement of fracture distribution and secondary fault strands in fault damage  
 1378 zones. *Journal of Geophysical Research: Solid Earth*, *116*(B3).
- 1379 Scholz, C., Molnar, P., & Johnson, T. (1972). Detailed studies of frictional sliding of

- 1380 granite and implications for the earthquake mechanism. *Journal of geophysical*  
 1381 *research*, 77(32), 6392–6406.
- 1382 Schreyer, H. L., & Chen, Z. (1986, 12). One-Dimensional Softening With Localiza-  
 1383 tion. *Journal of Applied Mechanics*, 53(4), 791-797. doi: 10.1115/1.3171860
- 1384 Segall, P., & Rice, J. R. (1995). Dilatancy, compaction, and slip instability of a  
 1385 fluid-infiltrated fault. *Journal of Geophysical Research: Solid Earth*, 100(B11),  
 1386 22155-22171. doi: 10.1029/95JB02403
- 1387 Sherratt, J., & Marchant, B. (1996). Nonsharp travelling wave fronts in the fisher  
 1388 equation with degenerate nonlinear diffusion. *Applied Mathematics Letters*,  
 1389 9(5), 33 - 38. doi: [https://doi.org/10.1016/0893-9659\(96\)00069-9](https://doi.org/10.1016/0893-9659(96)00069-9)
- 1390 Simo, J., & Taylor, R. (1985). Consistent tangent operators for rate-independent  
 1391 elastoplasticity. *Computer Methods in Applied Mechanics and Engineering*,  
 1392 48(1), 101 - 118. doi: [https://doi.org/10.1016/0045-7825\(85\)90070-2](https://doi.org/10.1016/0045-7825(85)90070-2)
- 1393 Sleep, N. H. (1995). Ductile creep, compaction, and rate and state dependent fric-  
 1394 tion within major fault zones. *Journal of Geophysical Research: Solid Earth*,  
 1395 100(B7), 13065–13080.
- 1396 Sleep, N. H. (1997). Application of a unified rate and state friction theory to the  
 1397 mechanics of fault zones with strain localization. *Journal of Geophysical Re-*  
 1398 *search: Solid Earth*, 102(B2), 2875-2895. doi: 10.1029/96JB03410
- 1399 Stathas, A., & Stefanou, I. (2022). The role of viscous regularization in dynamical  
 1400 problems, strain localization and mesh dependency. *Computer Methods in Ap-*  
 1401 *plied Mechanics and Engineering*, 388, 114185. doi: [https://doi.org/10.1016/j](https://doi.org/10.1016/j.cma.2021.114185)  
 1402 [.cma.2021.114185](https://doi.org/10.1016/j.cma.2021.114185)
- 1403 Tchalenko, J. (1970). Similarities between shear zones of different magnitudes. *Geo-*  
 1404 *logical Society of America Bulletin*, 81(6), 1625–1640.
- 1405 Templeton, E. L., & Rice, J. R. (2008). Off-fault plasticity and earthquake rup-  
 1406 ture dynamics: 1. dry materials or neglect of fluid pressure changes. *Journal of*  
 1407 *Geophysical Research: Solid Earth*, 113(B9).
- 1408 Thielmann, M. (2018). Grain size assisted thermal runaway as a nucleation  
 1409 mechanism for continental mantle earthquakes: Impact of complex rhe-  
 1410 ologies. *Tectonophysics*, 746, 611–623. doi: [https://doi.org/10.1016/](https://doi.org/10.1016/j.tecto.2017.08.038)  
 1411 [j.tecto.2017.08.038](https://doi.org/10.1016/j.tecto.2017.08.038)
- 1412 Thielmann, M., Rozel, A., Kaus, B., & Ricard, Y. (2015). Intermediate-depth earth-

- 1413           quake generation and shear zone formation caused by grain size reduction and  
1414           shear heating. *Geology*, *43*(9), 791. doi: 10.1130/G36864.1
- 1415   Triantafyllidis, N., & Aifantis, E. C. (1986). A gradient approach to localization of  
1416           deformation. i. hyperelastic materials. *Journal of Elasticity*, *16*(3), 225–237.
- 1417   Ulm, F.-J., Coussy, O., & Bažant, Z. P. (1999). The “chunnel” fire. i: Chemoplas-  
1418           tic softening in rapidly heated concrete. *Journal of engineering mechanics*,  
1419           *125*(3), 272–282.
- 1420   Van den Ende, M., Chen, J., Ampuero, J.-P., & Niemeijer, A. (2018). A comparison  
1421           between rate-and-state friction and microphysical models, based on numerical  
1422           simulations of fault slip. *Tectonophysics*, *733*, 273–295.
- 1423   Vardoulakis, I. (1980). Shear band inclination and shear modulus of sand in biax-  
1424           ial tests. *International journal for numerical and analytical methods in geome-*  
1425           *chanics*, *4*(2), 103–119.
- 1426   Vermeer, P. (1990). The orientation of shear bands in biaxial tests. *Geotechnique*,  
1427           *40*(2), 223–236.
- 1428   Veveakis, E., Poulet, T., & Alevizos, S. (2014). Thermo-poro-mechanics of chemi-  
1429           cally active creeping faults: 2. transient considerations. *Journal of Geophysical*  
1430           *Research: Solid Earth*, *119*(6), 4583–4605.
- 1431   Viesca, R. C. (2016a). Self-similar slip instability on interfaces with rate-and state-  
1432           dependent friction. *Proceedings of the Royal Society A: Mathematical, Physical*  
1433           *and Engineering Sciences*, *472*(2192), 20160254.
- 1434   Viesca, R. C. (2016b). Stable and unstable development of an interfacial sliding in-  
1435           stability. *Physical Review E*, *93*(6), 060202.
- 1436   Wolfram Research, Inc. (2017). *Mathematica, Version 11.1.1.0.* (Champaign, IL,  
1437           2017)
- 1438   Wu, J.-Y. (2017). A unified phase-field theory for the mechanics of damage and  
1439           quasi-brittle failure. *Journal of the Mechanics and Physics of Solids*, *103*, 72–  
1440           99.
- 1441   Wu, Y., Xing, X., & Ye, Q. (2006, 09). Stability of travelling waves with algebraic  
1442           decay for n-degree fisher-type equations. *Discrete and Continuous Dynamical*  
1443           *Systems*, *16*. doi: 10.3934/dcds.2006.16.47